Atomistic Modeling and Analysis of Hydride Phase Transformation in Palladium Nanoparticles

X. Sun, M.P. Ariza, M. Ortiz, K.G. Wang

PII: S0022-5096(18)30689-6
DOI: https://doi.org/10.1016/j.jmps.2019.01.006
Reference: MPS 3541

To appear in: *Journal of the Mechanics and Physics of Solids*

Received date: 12 August 2018
Revised date: 6 January 2019
Accepted date: 6 January 2019

Please cite this article as: X. Sun, M.P. Ariza, M. Ortiz, K.G. Wang, Atomistic Modeling and Analysis of Hydride Phase Transformation in Palladium Nanoparticles, *Journal of the Mechanics and Physics of Solids* (2019), doi: https://doi.org/10.1016/j.jmps.2019.01.006

Atomistic Modeling and Analysis of Hydride Phase Transformation in Palladium Nanoparticles

X. Sun[a], M. P. Ariza[b], M. Ortiz[c], K. G. Wang[a,*]

[a]*Department of Aerospace and Ocean Engineering, Virginia Polytechnic Institute and State University, Blacksburg, VA 24061, United States*
[b]*Escuela Técnica Superior de Ingeniería, Universidad de Sevilla, Sevilla 41092, Spain*
[c]*Division of Engineering and Applied Science, California Institute of Technology, Pasadena, CA 91125, United States*

Abstract

Palladium-hydrogen (Pd-H) is a prototypical system for studying solute-induced phase transformation in various energy conversion and storage applications. While the behaviors of bulk Pd-H have been studied extensively, the detailed atomic picture of hydride phase transformation within individual Pd nanoparticles is still unclear. In this work, we employ a novel atomistic computational model, referred to as Diffusive Molecular Dynamics (DMD), to characterize the H absorption dynamics in Pd nanoparticles of spherical, octahedral and cubic shapes. The DMD model couples a non-equilibrium thermodynamic model with a discrete diffusion law, which allows it to reach diffusive time scales with atomic resolution. The model is capable of capturing the propagation of an atomistically sharp hydride phase boundary. A remarkable feature of the phase boundary structure that is predicted by the calculations is the emergence of misfit dislocations distributed over the interface. These dislocations relieve the elastic residual stresses induced by the change of volume that accompanies the phase transformation. Shape effects are also investigated in this work. More specifically, in both spherical and octahedral nanoparticles, we observe stacking faults during the H absorption process while the phase boundary in the cubic nanoparticle remains coherent. The spatial distribution of the stacking faults in the spherical sample is investigated in detail using an elastic core-shell model. We also identify the mechanisms that enable the movement of the stacking faults as they track the propagation of the phase boundary. Finally, we find that the rate of H absorption is reduced by the formation and movement of the stacking faults.

Keywords: Hydrogen Absorption, Palladium Nanoparticles, Phase Transformation, Misfit Dislocations, Diffusive Molecular Dynamics

1. Introduction

Solute-induced phase transformation is a fundamental process in various energy conversion and storage applications. For example, the operation of lithium-ion batteries relies on a reversible phase transformation in the cathodic material (e. g., Li_xCoO_2, Li_xFePO_4), induced by the diffusion of lithium ions [1, 2]. Similarly, the storage of hydrogen in metals relies on the phase transformation of the hydride (e. g., MgH_x, $NaAlH_x$), induced by the diffusion of hydrogen atoms [3, 4, 5]. For these applications, there has been a continuous push towards nanostructured systems, as they hold promise for accelerating the charging and discharging process, increasing the energy and power density, and extending the life cycle [1, 6, 7, 8].

The palladium-hydrogen (Pd-H) system is a prototypical model for studying solute-induced phase transformation, as it allows for relatively fast reaction kinetics at easily accessible temperatures and pressures [9]. The Pd-H system exhibits two distinct phases at room temperature: the dilute α phase at low H concentration (up to $PdH_{0.015}$), and the β phase at high H concentration ($PdH_{0.6}$ and above). In both phases, the Pd lattice maintains the face-centered cubic (FCC) structure, while the H atoms occupy the octahedral

*Corresponding author
Email address: kevinwgy@vt.edu (K. G. Wang)

interstitial sites. Attendant to the α/β phase transformation, there is a lattice expansion with 10.4% increase in volume which may lead to the formation of misfit dislocations.

While the behavior of Pd-H is well-understood in the bulk, the phase transformation dynamics within nanostructured Pd-H systems remains an active area of research [7, 10, 11, 12, 13, 14, 15, 16, 17, 18]. In this regard, a few recent experiments suggest that in nanosized particles, the phase transformation is driven by the propagation of an atomistically sharp phase boundary at a speed as low as 1 nm/s. For example, by scanning transmission electron microscopy (STEM), Narayan *et al.* observed the propagation of a sharp α/β phase boundary in individual Pd nanocubes with edge lengths between 20 nm and 40 nm [16]. Using coherent X-ray diffractive imaging, Ulvestad *et al.* measured the evolution of strain within individual Pd nanocubes between 60 nm and 100 nm, which also indicates a sharp α/β phase transformation [14, 17]. Beyond the overall transformation mechanism, other unresolved issues include the morphology of the phase boundary [11, 16, 17], the effect of particle shape and lattice orientation [12], and the interaction of phase boundary with preexisting defects [15].

In this work, we apply a novel computational method, referred to as Diffusive Molecular Dynamics (DMD), to investigate the detailed dynamics of hydride phase transformation in Pd nanoparticles, focusing on the two-way interaction between the motion of the phase boundary and the formation and evolution of misfit dislocations. DMD is a new paradigm for simulating long-term diffusive mass and heat transport while maintaining full atomic resolution [19, 20, 21, 22, 18, 23, 24, 25, 26, 27, 28]. The basic idea is to couple a calibrated empirical kinetic model for the evolution of lattice site occupancy with a non-equilibrium statistical thermodynamics model that supplies the requisite driving forces for kinetics. The basic assumption underlying DMD is that the time scale of diffusion is much larger than that of microscopic state transitions. Therefore at an intermediate time scale, the microscopic state variables can be considered as random variables. In comparison to the established atomistic methods (e. g., Molecular Dynamics (MD), transition state theory based accelerated MD [29], and kinetic Monte Carlo [30]), DMD has a larger simulation time window as it does not explicitly resolve thermal vibrations or the individual microscopic state transitions. DMD has been applied to nanoindentation and sintering [19, 23], dislocation extension [24], nanovoid growth [20, 22, 27], heat conduction in nanowires [31] and solute-defect interactions [21, 32]. Recently, DMD has been employed to study the effect of particle size on the hydrogenation process of cubic Pd nanoparticles [33]. A one-dimensional version has also been applied to simulate H diffusion in Pd nanofilms, in which the Pd subsystem was assumed to be rigid [18].

The large time window and atomic resolution of DMD makes it an excellent tool for studying hydride phase transformation within Pd nanoparticles, which unfolds on a time scale of minutes to hours. Therefore, the key insights obtained in this paper are the detailed H absorption dynamics and the induced lattice deformation process through DMD simulations. In this paper, we start with a brief summary of assumptions and model equations underlying DMD, in Section 2. Then, we describe the setup of the numerical H absorption experiments under consideration in Section 3. Specifically, we consider three nanoparticles of approximately the same volume ($3,800 \pm 90$ nm^3), yet of different shapes, including a spherical particle exemplifying smooth geometries, and an octahedral and a cubic particles that have flat faces and sharp edges and corners. The octahedral particle is designed such that all of its 8 faces are on $\{111\}$ planes, which are the most common slip planes in FCC crystals. By contrast, the cubic particle is designed with their faces on $\{100\}$ planes. Next, we discuss the results of the numerical experiments, including the propagation of the α/β phase boundary (Section 4), the attendant dynamics of interfacial misfit dislocations and stacking faults (Section 5), and the rate of H absorption (Section 6). In order to explain the observed stacking fault distribution, we formulate a simple elastic core-shell model amenable to analytical solution. Then, a comparison between MD and DMD simulation results is provided in Section 7. Finally, we provide a summary and concluding remarks in Section 8.

2. Methodology

The behavior of Pd-H depends sensitively on processes that pertain to different time scales, ranging from the thermal vibrations of Pd and H atoms on the order of femtosecond (Fig. 1(a)), to the propagation of a hydride phase boundary in Pd nanoparticles on the order of second or even longer time scales (Fig. 1(c)). To address this significant gap between different time scales, the main assumption behind the DMD theory is that when viewed on an intermediate time scale, much larger than that of thermal vibration, the microscopic

state variables of an atomic site, e. g., instantaneous position, momentum and occupancy, can be regarded as random variables described by probability density functions, as illustrated in Fig. 1(b). This intermediate time scale may correspond to one time-step of DMD simulation (e. g., on the order of millisecond in this work). As a result, the DMD theory focuses on solving the time-dependent statistical measures of these random variables, e. g., mean and variance. For the sake of completeness and convenience, in this section we summarize the specific version of DMD theory for the Pd-H system. A more general DMD theory can be found in Ref. [21].

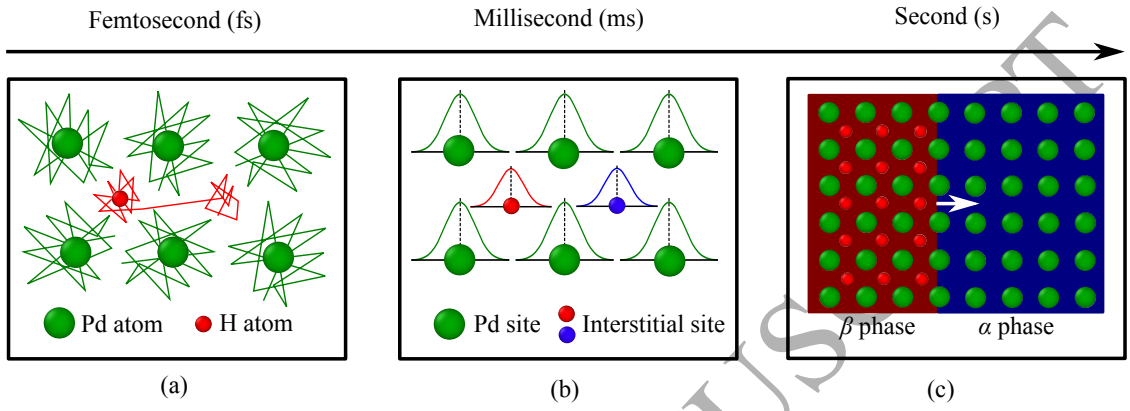

Figure 1: Schematic illustration of time scale separation: (a) thermal vibrations of atoms on the order of femtosecond, (b) one time-step of DMD simulations on the order of millisecond, and (c) propagation of phase boundary on the order of second.

2.1. Non-equilibrium thermodynamics model

We consider a binary Pd-H system consisting of host sites that are occupied by Pd atoms and interstitial sites that can be either occupied by H atoms or unoccupied. For ease of reference, the sets of host and interstitial sites are denoted by I_{Pd} and I_{H}, respectively. On each interstitial site $i \in I_{\mathrm{H}}$, we introduce an occupancy function n_i, defined as

$$n_i = \begin{cases} 1 & \text{if the site } i \text{ is occupied by a H atom,} \\ 0 & \text{if the site } i \text{ is unoccupied.} \end{cases} \tag{1}$$

The instantaneous position and momentum of site i are denoted by $\boldsymbol{q}_i$ and $\boldsymbol{p}_i$, respectively. Based on the assumption of scale separation and the ergodic hypothesis, these microscopic state variables can be viewed as random variables that have a joint probability distribution characterized by density function $\rho\big(\{\boldsymbol{q}\},\{\boldsymbol{p}\},\{n\}\big)$, where $\{\boldsymbol{q}\} = \{\boldsymbol{q}_i : i \in I_{\mathrm{Pd}} \cup I_{\mathrm{H}}\}$, $\{\boldsymbol{p}\} = \{\boldsymbol{p}_i : i \in I_{\mathrm{Pd}} \cup I_{\mathrm{H}}\}$ and $\{n\} = \{n_i : i \in I_{\mathrm{H}}\}$. We assume that the statistics of the system follows Jaynes' principles of maximum entropy [34, 35]. Therefore, the probability density function ρ is calculated by maximizing the information-theoretical entropy

$$S[\rho] = -k_{\mathrm{B}}\langle \log \rho \rangle, \tag{2}$$

with local constraints on each site

$$\begin{cases} \langle h_i \rangle = e_i, & i \in I_{\mathrm{Pd}} \cup I_{\mathrm{H}}, \\ \langle n_i \rangle = x_i, & i \in I_{\mathrm{H}}, \end{cases} \tag{3}$$

where k_{B} is the Boltzmann constant, and $\langle\cdot\rangle$ denotes the expectation operator. Here, h_i, e_i and x_i denote the local Hamiltonian, particle energy and H atomic fraction of site i, respectively. Using the method of Lagrange multipliers, we have

$$\rho = \frac{1}{\Xi} \mathrm{e}^{-\{\beta\}^{\mathrm{T}}\{h\}+\{\gamma\}^{\mathrm{T}}\{n\}}, \tag{4}$$

where Ξ is the partition function, and $\{\beta\}$ and $\{\gamma\}$ are Lagrange multipliers. In comparison with equilibrium statistical thermodynamics, Eq. (4) can be interpreted as a non-equilibrium generalization of the Gibbs

grand-canonical probability density function. Also, $T_i = 1/(k_\mathrm{B}\beta_i)$ and $\mu_i = k_\mathrm{B}T_i\gamma_i$ can be defined as the absolute temperature and the chemical potential of atomic site i, respectively.

Since the Hamiltonian h_i is typically a nonlinear function, the exact calculation of the thermodynamic properties (e. g., e_i and Ξ) is generally impossible. Venturini *et al.* [21] proposed an approximation theory, in which the optimization problem is performed within a finite-dimensional trial space $\mathcal{P}_0$, spanned by a pre-specified class of trial Hamiltonians $\{h_0\}$. As a result, maximizing $\mathcal{S}[\rho]$ within $\mathcal{P}_0$ is equivalent to minimizing the mean field free entropy, i. e.,

$$\min_{\{\alpha\}} \ \mathcal{F}\big(\{\beta\},\{\gamma\};\{h_0\}\big) = k_\mathrm{B}\{\beta\}^\mathrm{T}\big\{\langle h - h_0\rangle_0\big\} - k_\mathrm{B}\log\Xi_0, \tag{5}$$

where $\{\alpha\}$ is a finite set of parameters that characterize $\{h_0\}$. $\langle\cdot\rangle_0$ denotes the expectation operator under the trial probability density function, and Ξ_0 is the trial partition function. We consider a uniform and constant temperature and apply the approximation theory with a trial Hamiltonian

$$h_{0i}(\boldsymbol{q}_i,\boldsymbol{p}_i,n_i;\ \bar{\boldsymbol{q}}_i,\sigma_i,\bar{\boldsymbol{p}}_i,\gamma_{0i}) = \begin{cases} \dfrac{k_\mathrm{B}T}{2\sigma_i^2}|\boldsymbol{q}_i-\bar{\boldsymbol{q}}_i|^2 + \dfrac{1}{2m_\mathrm{Pd}}|\boldsymbol{p}_i-\bar{\boldsymbol{p}}_i|^2, & \text{if } i\in I_\mathrm{Pd}, \\ \dfrac{k_\mathrm{B}T}{2\sigma_i^2}|\boldsymbol{q}_i-\bar{\boldsymbol{q}}_i|^2 + \dfrac{1}{2m_\mathrm{H}}|\boldsymbol{p}_i-\bar{\boldsymbol{p}}_i|^2 - k_\mathrm{B}T\gamma_{0i}n_i, & \text{if } i\in I_\mathrm{H}, \end{cases} \tag{6}$$

where T is the constant temperature. $\bar{\boldsymbol{q}}_i$, σ_i, $\bar{\boldsymbol{p}}_i$, and γ_{0i} are parameters that characterize the trial space. m_Pd and m_H denote the atomic mass of Pd and H, respectively. It can be shown that $\bar{\boldsymbol{q}}_i$ and σ_i are the mean and standard deviation of $\boldsymbol{q}_i$, respectively, whereas $\bar{\boldsymbol{p}}_i$ is the mean of $\boldsymbol{p}_i$. In Eq. (6), γ_{0i} indicates the dependence of chemical potential on H fraction x_i. Specifically, applying $\langle n_i\rangle_0 = x_i$ yields

$$\gamma_{0i} = \log\frac{x_i}{1-x_i} - \gamma_i. \tag{7}$$

Substituting Eqs. (6) and (7) into Eq. (5) gives

$$\begin{aligned} &\min_{\{\bar{\boldsymbol{q}}\},\{\sigma\},\{\bar{\boldsymbol{p}}\},\{x\}} \mathcal{F}\big(T,\{\gamma\};\{\bar{\boldsymbol{q}}\},\{\sigma\},\{\bar{\boldsymbol{p}}\},\{x\}\big) \\ &= \frac{1}{T}\langle V\rangle_0 + \frac{1}{2Tm_\mathrm{Pd}}\sum_{i\in I_\mathrm{Pd}}\bar{\boldsymbol{p}}_i^2 + \frac{1}{2Tm_\mathrm{H}}\sum_{i\in I_\mathrm{H}}x_i\bar{\boldsymbol{p}}_i^2 + \frac{3}{2}k_\mathrm{B}\sum_{i\in I_\mathrm{Pd}}\left(\log\frac{\hbar^2}{k_\mathrm{B}Tm_\mathrm{Pd}\sigma_i^2} - 1\right) \\ &+ \frac{3}{2}k_\mathrm{B}\sum_{i\in I_\mathrm{H}}\left(\log\frac{\hbar^2}{k_\mathrm{B}Tm_\mathrm{H}\sigma_i^2} + x_i - 2\right) + k_\mathrm{B}\sum_{i\in I_\mathrm{H}}\big(x_i\log x_i + (1-x_i)\log(1-x_i) - \gamma_i x_i\big), \end{aligned} \tag{8}$$

where $\hbar$ is the reduced Planck constant. $V\big(\{\boldsymbol{q}\},\{n\}\big)$ denotes the interatomic potential energy and its average is calculated by third-order Gaussian quadratures on a sparse grid [19]. Enforcing the first-order necessary condition with respect to $\bar{\boldsymbol{p}}_i$ yields $\bar{\boldsymbol{p}}_i = \boldsymbol{0}$. Enforcing the first-order necessary condition with respect to x_i yields

$$\gamma_i = \frac{3}{2} + \log\frac{x_i}{1-x_i} + \frac{1}{k_\mathrm{B}T}\frac{\partial\langle V\rangle_0}{\partial x_i}, \quad i\in I_\mathrm{H}, \tag{9}$$

which shows that the atomic chemical potential depends on both the atomic H fraction and the interatomic potential energy. As a result, the optimization problem simplifies to

$$\begin{aligned} &\min_{\{\bar{\boldsymbol{q}}\},\{\sigma\}} \mathcal{F}\big(T,\{\gamma\};\{\bar{\boldsymbol{q}}\},\{\sigma\},\{x\}\big) \\ &= \frac{1}{T}\langle V\rangle_0 + \frac{3}{2}k_\mathrm{B}\sum_{i\in I_\mathrm{Pd}}\left(\log\frac{\hbar^2}{k_\mathrm{B}Tm_\mathrm{Pd}\sigma_i^2} - 1\right) + \frac{3}{2}k_\mathrm{B}\sum_{i\in I_\mathrm{H}}\left(\log\frac{\hbar^2}{k_\mathrm{B}Tm_\mathrm{H}\sigma_i^2} + x_i - 2\right) \\ &+ k_\mathrm{B}\sum_{i\in I_\mathrm{H}}\big(x_i\log x_i + (1-x_i)\log(1-x_i) - \gamma_i x_i\big). \end{aligned} \tag{10}$$

As a result, the non-equilibrium thermodynamics model formulated in Eq. (10) is employed to calculate the mean positions of atomic sites $\{\bar{\boldsymbol{q}}\}$ under the specific configuration of H fractions $\{x\}$, in order to capture the lattice deformation caused by solute atoms.

2.2. Discrete diffusion model

The thermodynamics model formulated in Eq. (10) is then coupled with a discrete kinetic law, which enforces the balance of mass at each interstitial site, i. e.,

$$\dot{x}_i = \sum_{j \neq i} J_{ij}, \quad i, j \in I_{\mathrm{H}}, \tag{11}$$

where J_{ij} denotes the *bondwise* mass flux from site j to site i, and satisfies $J_{ij} = -J_{ji}$. After a straightforward calculation, the internal entropy production rate from a pair of sites $\langle i, j \rangle$ is

$$\Sigma_{ij} = K_{ij} J_{ij}, \tag{12}$$

where

$$K_{ij} = -\frac{1}{T}(\mu_i - \mu_j) = -k_{\mathrm{B}}(\gamma_i - \gamma_j) \tag{13}$$

defines the discrete thermodynamic force corresponding to the discrete mass transport J_{ij}. Following Onsager's theory of kinetic relations [36], we employ a kinetic law of the general form

$$J_{ij} = -\frac{\partial \psi}{\partial K_{ij}}\big(\{K\}\big), \tag{14}$$

where $\psi\big(\{K\}\big)$ is a discrete kinetic potential, which needs to be modeled. Venturini *et al.* [21] proposed a simple kinetic potential, by assuming linear relation between mass flux J_{ij} and driving force K_{ij}. The resulting discrete mass transport J_{ij} is

$$J_{ij} = B_0 \frac{x_i + x_j}{2} K_{ij}, \tag{15}$$

where B_0 denotes the bondwise diffusion coefficient, which can be calibrated to reproduce the speed of diffusion observed in experiments. As a result, we have

$$\dot{x}_i = -k_{\mathrm{B}} B_0 \sum_{j \neq i} \frac{x_i + x_j}{2} (\gamma_i - \gamma_j), \quad i, j \in I_{\mathrm{H}}. \tag{16}$$

For simplicity, but without loss of generality, in our DMD simulations we restrict diffusive transport within one shell of neighbors. The above discrete kinetic law has been validated against the classical lattice random walk model for the long-term dynamics of a single H atom in Pd [37]. It has also been applied to study surface segregation in AuAg alloys [38]. Moreover, similar bondwise flux functions have been employed to simulate spin-diffusion in a one-dimensional binary alloy [39]. It is also noteworthy that the simplified kinetic relation formulated in Eq. (16) is regarded as an *empirical* one. While the parameter B_0 is assumed to be independent of a site's local atomic configuration for simplicity, the chemical potential γ_i formulated in Eq. (9) takes into account detailed atomic configurations (i. e., site positions and H fractions). As a result, mass transport is locally modified, e. g., in the vicinity of a phase interface and lattice defects.

2.3. Implementation details

Our DMD model couples a nonlinear optimization problem, i. e., Eq. (10), with a first-order, nonlinear ordinary differential equation (ODE), i. e., Eq. (16). We solve this coupled system by discretizing the ODE using an explicit time integrator (e. g., forward-Euler), and solving the optimization problem once per time step using a quasi-Newton Broyden-Fletcher-Goldfarb-Shanno (BFGS) method [40]. We have developed a DMD solver, which is parallelized with Message Passing Interface (MPI), using the PETSc/TAO library [41] for large-scale simulations on computer clusters with distributed memory. Details of the solutions of the equations and the computation procedure of DMD can be found in Ref. [37].

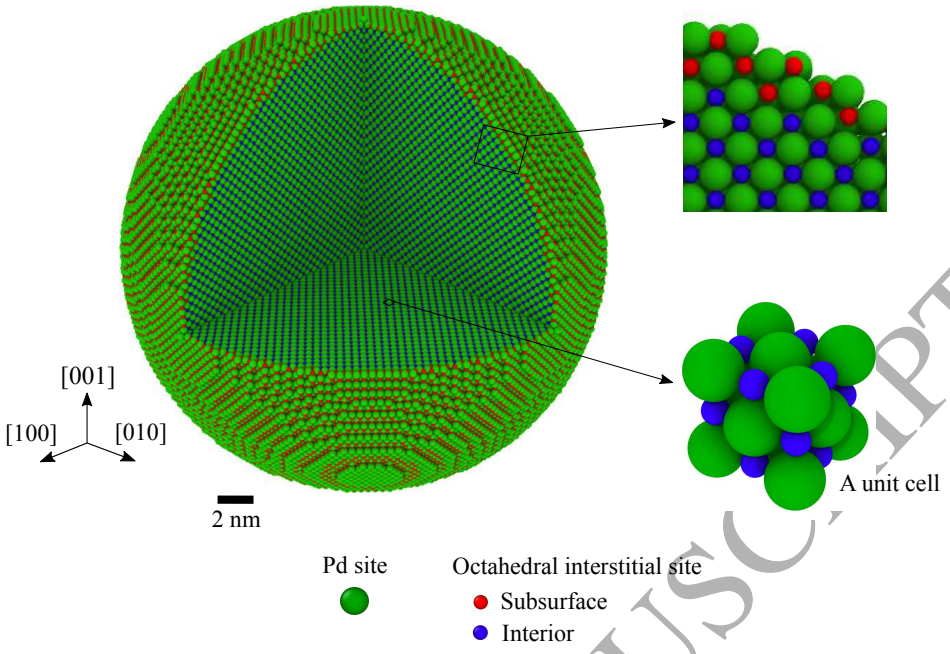

Figure 2: Computational model of the spherical particle with a diameter of 19.5 nm.

3. Setup of numerical experiments

We build three nanoparticles of different shapes, including a sphere, an octahedron with faces on {111} planes, and a cube with faces on {100} planes. The three particles are designed to have approximately the same volume, that is, $3,800 \pm 90$ nm^3 and $516,000 \pm 8,000$ atomic sites (including the octahedral interstitial sites that can be occupied by H atoms). The sphere has a diameter of 19.5 nm. The octahedron and the cube have an edge length of 19.9 nm and 15.6 nm, respectively. As an example, Fig. 2 shows the computational model of the spherical particle. All the three particles are single crystals.

Under a gas-phase condition, the absorption of H_2 by Pd begins with the dissociation of H_2 into H atoms on the surface of the Pd specimen (i. e., adsorption). The H atoms penetrate into a subsurface layer, then move into the interior of the Pd specimen, occupying the octahedral interstitial sites of the FCC lattice [42, 13, 43]. Palladium hydride (Pd-H) exists in two phases, namely a low H concentration α phase and a high H concentration β phase. Both phases have an FCC lattice, with different lattice constants (3.895 Å versus 4.025 Å [44]). Previous studies suggest that the H_2 partial pressure required to achieve subsurface saturation is lower than that required to initiate the α/β phase transformation in the interior [45, 46, 47]. Also, the saturation of H in the subsurface layer is achieved much faster than the diffusion of H into the interior of a Pd specimen. Therefore, in our DMD analysis, we simulate these two processes separately in two steps, as described in Algorithm 1.

Specifically, we assume that the Pd particle is subjected to a constant H_2 partial pressure, and hence a constant external chemical potential μ_{env}. In the first step of the analysis, we determine the distribution of H in the subsurface layer and the resulting lattice deformation of the particle, when this layer has just reached equilibrium with the external H environment. We assume that the subsurface layer covers the entire particle with a uniform thickness, following the spherical-shell mechanism that has been used to interpret experimental results in a few previous studies [11, 47]. We set $\gamma_i = \mu_{\text{env}}/(k_{\text{B}}T)$ (i. e., $\mu_i = \mu_{\text{env}}$) for all the interstitial sites within the subsurface layer and $x_i = 0$ for all the interstitial sites in the interior of the particle. Then, we solve Eq. (9) using fixed-point iteration, to obtain the equilibrium distribution of x_i within the subsurface layer, and minimize the free entropy in Eq. (10) to obtain the values of $\{\bar{\boldsymbol{q}}\}$ and $\{\sigma\}$ in the particle. We also note that the nucleation of the β phase within the subsurface may be inherently a stochastic process that depends on random localized thermal fluctuations. Nonetheless, due to the aforementioned time separation between subsurface saturation and H diffusion into the interior, we deem the calculation result of

Algorithm 1 Solution of the DMD equations in the two-step calculation.

Input: $\{x_i^0 : i \in I_{\rm INT}\}$ (initial H fractions in the interior), $\mu_{\rm env} = k_{\rm B}T\gamma_{\rm env}$ (environmental chemical potential)
Begin
First step: with $\{x_i^0 : i \in I_{\rm INT}\}$ fixed
  Fixed-Point Iteration: set $\{x_i^0 : i \in I_{\rm SURF}\}$ (initial guess of H fractions in the subsurface layer)
  for $l \leftarrow 0;\ l < l_{\max}$ **do**
    $\{x\}^l \leftarrow \{x_i^l : i \in I_{\rm SURF}\} \cup \{x_i^0 \in I_{\rm INT}\}$
    minimize $\mathcal{F}\big(\{\bar{\boldsymbol{q}}\}, \{\sigma\}, \{x\}^l\big) \Rightarrow \{\bar{\boldsymbol{q}}\}^l, \{\sigma\}^l$
    $$x_i^{l+1} \leftarrow \frac{\exp\left(\gamma_{\rm env} - \frac{3}{2} - \frac{1}{k_{\rm B}T}\frac{\partial\langle V\rangle_0}{\partial x_i}\Big|^l\right)}{1+\exp\left(\gamma_{\rm env} - \frac{3}{2} - \frac{1}{k_{\rm B}T}\frac{\partial\langle V\rangle_0}{\partial x_i}\Big|^l\right)}, \quad \forall i \in I_{\rm SURF}$$
    if $\sum_{i\in I_{\rm SURF}} \left(x_i^{l+1} - x_i^l\right)^2 < \epsilon_1$ **then**
      break
    $l \leftarrow l+1$
  Output: the final results, i. e., $\{x_i^* : i \in I_{\rm SURF}\},\ \{\bar{\boldsymbol{q}}\}^*,\ \{\sigma\}^*$
Second step: with $\{x_i^* : i \in I_{\rm SURF}\}$ and $\{\gamma_i \leftarrow \gamma_{\rm env} : i \in I_{\rm SURF}\}$ fixed
  $t = 0,\ n = 0$
  $\{\bar{\boldsymbol{q}}\}^0 \leftarrow \{\bar{\boldsymbol{q}}\}^*,\ \{\sigma\}^0 \leftarrow \{\sigma\}^*$
  while $t < t_{\max}$ **do**
    Temporal Integration: with $\{\bar{\boldsymbol{q}}\}^n$ and $\{\sigma\}^n$ fixed, solve Eq. (16) by forward-Euler $\Rightarrow \{x\}^{n+1}$
    Begin
      $$\gamma_i^n \leftarrow \frac{3}{2} + \log\frac{x_i^n}{1-x_i^n} + \frac{1}{k_{\rm B}T}\frac{\partial\langle V\rangle_0}{\partial x_i}\Big|^n, \quad \forall i \in I_{\rm INT}$$
      $\{\gamma\}^n \leftarrow \{\gamma_i^n : i \in I_{\rm INT}\} \cup \{\gamma_i \leftarrow \gamma_{\rm env} : i \in I_{\rm SURF}\}$
      solve Eq. (16) for one time-step, i. e.,
      $$x_i^{n+1} \leftarrow x_i^n - k_{\rm B}B_0\Delta t \sum_{j\in I_{\rm H}, j\neq i} \frac{1}{2}(x_i^n + x_j^n)(\gamma_i^n - \gamma_j^n), \quad \forall i \in I_{\rm INT}$$
      $\{x\}^{n+1} \leftarrow \{x_i^{n+1} : i \in I_{\rm INT}\} \cup \{x_i^* : i \in I_{\rm SURF}\}$
    End
    Optimization: with $\{x\}^{n+1}$ fixed, solve Eq. (10) by BFGS $\Rightarrow \{\bar{\boldsymbol{q}}\}^{n+1}, \{\sigma\}^{n+1}$
    Begin
      $\boldsymbol{X} \equiv \big\{\{\bar{\boldsymbol{q}}\}, \{\sigma\}\big\}$
      $\mathcal{F}(\boldsymbol{X}) \equiv \mathcal{F}\big(\{\bar{\boldsymbol{q}}\}, \{\sigma\}, \{x\}^{n+1}\big)$
      for $k \leftarrow 0, \boldsymbol{X}^0 \leftarrow \big\{\{\bar{\boldsymbol{q}}\}^n, \{\sigma\}^n\big\};\ k < k_{\max}$ **do**
        compute approximate Hessian matrix $\mathcal{H}^k$
        $\Delta\boldsymbol{X} \leftarrow -(\mathcal{H}^k)^{-1}\nabla\mathcal{F}(\boldsymbol{X}^k)$
        determine step size τ by line search
        $\boldsymbol{X}^{k+1} \leftarrow \boldsymbol{X}^k + \tau\Delta\boldsymbol{X}$
        if $\big|\mathcal{F}(\boldsymbol{X}^{k+1}) - \mathcal{F}(\boldsymbol{X}^k)\big| < \epsilon_2$ or $\dfrac{\big|\mathcal{F}(\boldsymbol{X}^{k+1}) - \mathcal{F}(\boldsymbol{X}^k)\big|}{\big|\mathcal{F}(\boldsymbol{X}^k)\big|} < \epsilon_3$ **then**
          break
        $k \leftarrow k+1$
    End
    $t \leftarrow t + \Delta t,\ n \leftarrow n+1$
  Output: the results at each time step, i. e., $\{\bar{\boldsymbol{q}}\}^n,\ \{\sigma\}^n,\ \{x\}^n,\ \{\gamma\}^n$
End

this step to be the final equilibrium state of subsurface nucleation.

Next, we assume that throughout the H absorption process, the subsurface layer remains in equilibrium with the external H environment. Therefore, in the second step, we fix $\gamma_i = \mu_{\text{env}}/(k_{\text{B}}T)$ and x_i (obtained in the first step) in the subsurface layer, and apply the dynamic, deformation-diffusion coupled DMD model to predict the diffusion of H from the subsurface to the interior of the Pd particles. This setting is also consistent with the aforementioned spherical-shell mechanism.

We employ the embedded atom method (EAM) potential developed by Zhou *et al.* [48], which is capable of capturing the separation of α and β phases [18]. We set temperature $T = 300$ K. The thickness of the subsurface layer, denoted by τ, has been estimated to be of the order of 0.1 nm to 1 nm — for example, 0.3 nm using an equilibrium Monte Carlo method [49] and 1.03 nm using a phase-field model [50]. In this work, we set $\tau = 0.3$ nm. Moreover, the functional relationship between the H_2 partial pressure and the corresponding chemical potential μ_{env} is unclear. We have conducted a parameter study, and found that the α/β phase transformation is achieved when $\mu_{\text{env}} > -2.25$ eV. The results presented in this paper are obtained with $\mu_{\text{env}} = -2.0$ eV, and in this case we get full coverage, i. e., $x_i = 1$, over the subsurface layer in all the three particles after the first step calculation. Further, we have calibrated the atomic diffusivity coefficient B_0 to reproduce the experimental measurement of the speed of H absorption obtained in a similar setting [16], which yields $B_0 = 500.0$ K/(eV $\cdot$ s). The simulation results in the absorption process, i. e., the second step of DMD analysis, will be discussed in detail in the following sections.

The DMD analyses presented in this paper are performed using the BlueRidge supercomputer (Cray CS-300, with Intel Sandy Bridge CPUs) at Virginia Tech [51]. Each analysis consumes approximately $80,000$ CPU hours. The simulation results are visualized using OVITO [52].

4. Propagation of phase boundary

We begin by examining the diffusion of H during the absorption process. Figure 3 presents the result for the spherical particle. At 4.5 s, a spherical shell with high H concentration — corresponding to the β phase of Pd-H — has formed under the surface of the particle. By contrast, the interior of the particle still has low H concentration (close to 0), which can be interpreted as the α phase. The α and β phases are separated by a sharp boundary consisting of only a few layers of atomic sites, with a thickness of approximately 0.5 nm. This phase boundary is extracted and visualized at three different time instances. At the beginning (e. g., 4.5 s), it has a spherical shape. As time increases, the phase boundary propagates towards the center of the particle, and gradually deforms into a polyhedron with 8 triangular faces and 6 square faces (i. e., a cuboctahedron). The triangular and square faces have normals in $\langle 111\rangle$- and $\langle 100\rangle$-directions, respectively.

The morphological evolution of the phase boundary indicates that H atoms "move" slower along the radial lines that pass through the corners and edges of the polyhedron. Notably, misfit dislocations are also observed near these geometric singularities (the result will be discussed in the next section). Therefore, it is likely that the misfit dislocations have slowed down the propagation of the phase boundary. This can be explained by the fact that a semi-coherent phase boundary leads to less space in the α phase Pd lattice compared to a coherent one. This mechanism is schematically illustrated in Fig. 4.

Figures 5 and 6 present the results for the octahedral and cubic particles, respectively. In these two particles, we also observe the formation of an atomistically sharp α/β phase boundary, which advances towards the center of the particle. The shape of the phase boundary changes in time. In the octahedral particle, the phase boundary evolves from a sharp octahedron into a truncated one. The locations of sharp edges retained in the truncated octahedron coincide with the locations of misfit dislocations, which again indicates that misfit dislocations may slow down H diffusion. On the other hand, misfit dislocation is not observed in the cubic particle. In this case, the phase boundary changes gradually from a cube to a sphere. In other words, the sharp corners and edges of the initial phase boundary are gradually smeared. This can be explained as a mechanism to minimize the interfacial energy of the phase boundary.

For all the three different shapes, the DMD analysis indicates that the H absorption process is dominated by the formation and propagation of an atomistically sharp α/β phase boundary. This prediction agrees with the findings of a few recent experimental studies on individual Pd particles [16, 14]. Specifically, Narayan *et al.* [16] tested nanocubes with edge length between 20 nm and 40 nm, and observed sharp diffraction contrast in STEM (scanning transmission electron microscopy) images. Ulvestad *et al.* [14] also tested nanocubs with

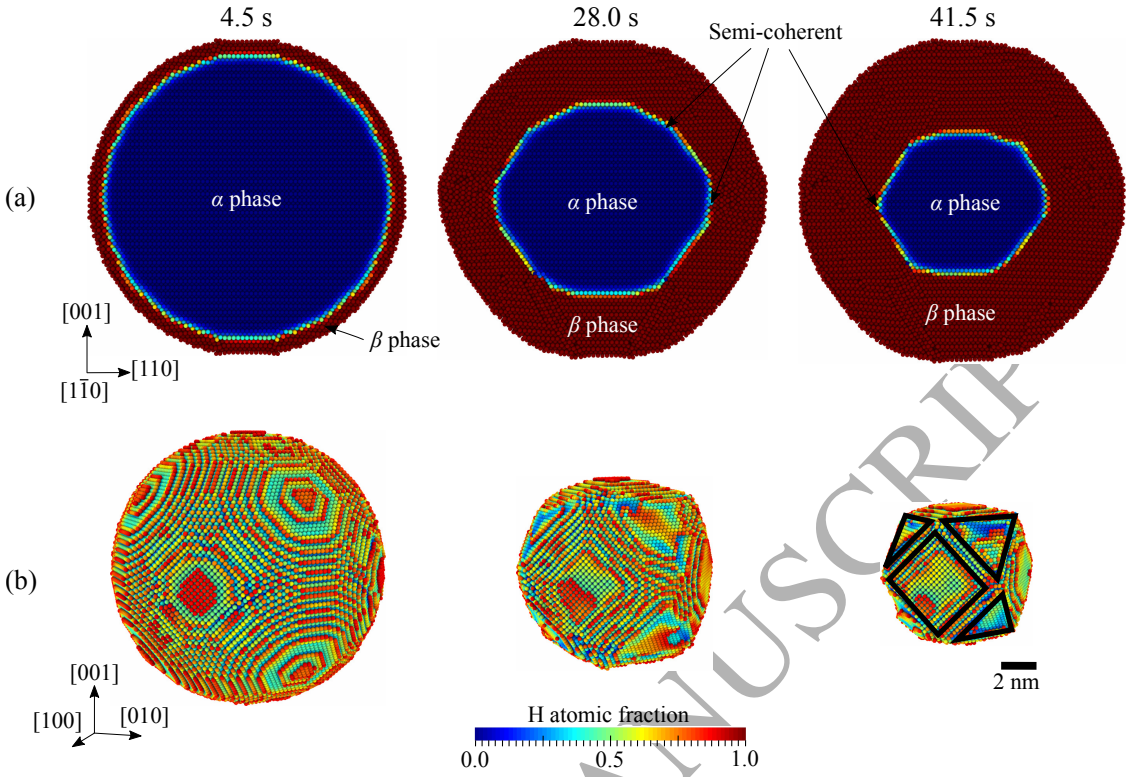

Figure 3: Hydride phase boundary in the spherical particle at three different time instances: (a) H fraction on the middle [1$\bar{1}$0] cross-section, and (b) a perspective view of the extracted phase boundary.

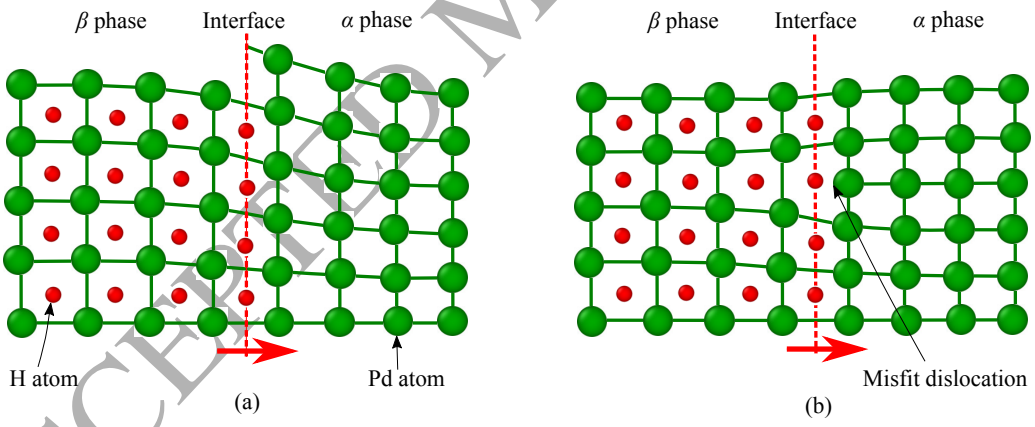

Figure 4: Schematic illustration of (a) a coherent and (b) a semi-coherent hydride phase boundary.

edge lengths between 60 nm and 100 nm, and observed the disappearance of Bragg electron density in a region from the density field of the Pd nanoparticles.

The separation of α and β phases by a sharp interface can be explained using the equilibrium relation between the chemical potential and the H atomic fraction. Figure 7 plots this equilibrium relation, using the EAM potential of Zhou *et al.* [48] and Eq. (9). The chemical potential function has two local extrema: one at a low H fraction of 0.25, the other at a high H fraction of 0.81. These two extreme values can be interpreted as the critical concentrations for the α and β phases of Pd-H, predicted by the specific interatomic potential. Since the H absorption is driven by the difference of chemical potential between different phases, this feature of double extrema likely leads to the formation and propagation of the sharp phase boundary.

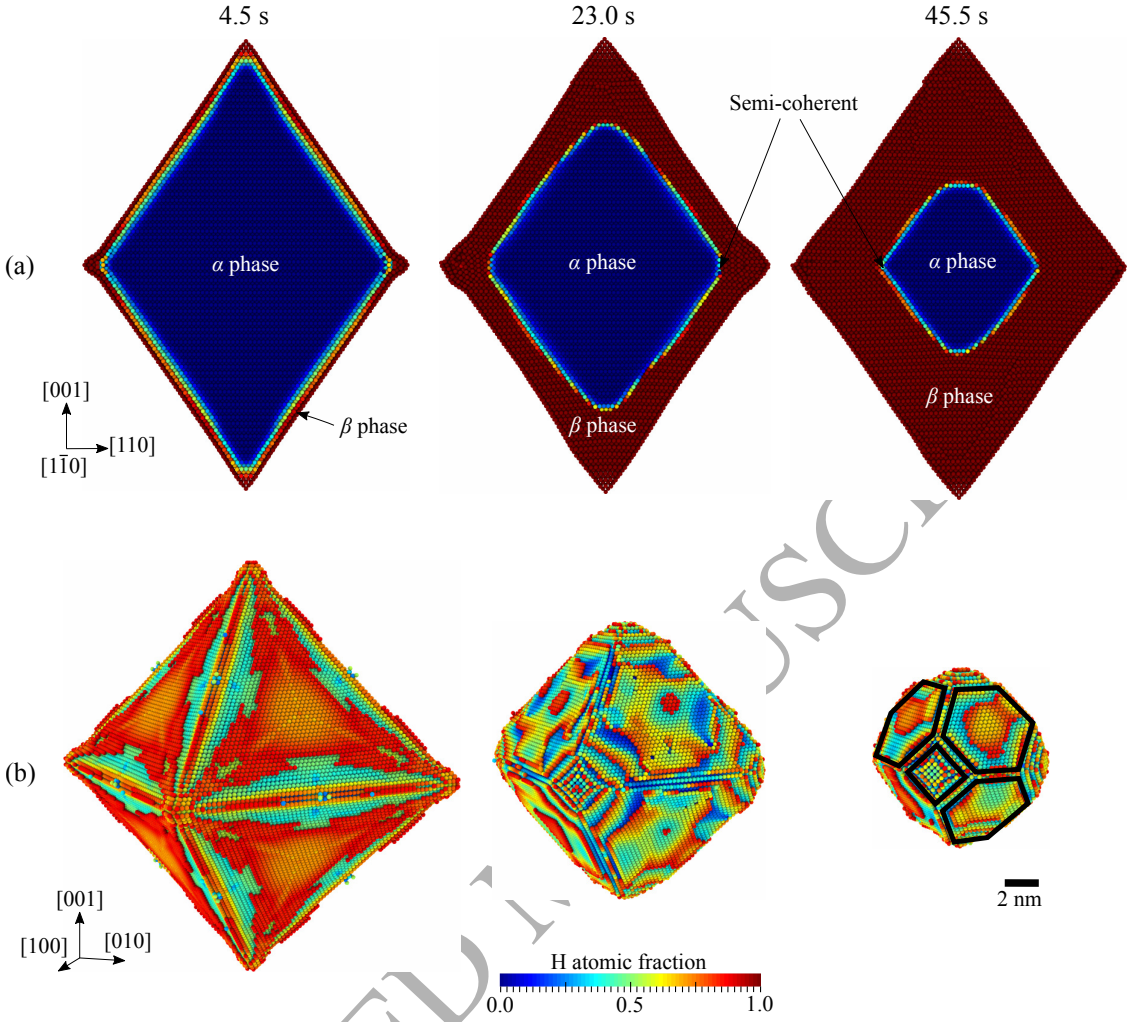

Figure 5: Hydride phase boundary in the octahedral particle at three different time instances: (a) H fraction on the middle [1$\bar{1}$0] cross-section, and (b) a perspective view of the extracted phase boundary.

Further, the chemical potential can also be related to the pressure of H_2 gas. In this regard, the profile of the chemical potential function is consistent with the pressure-composition isotherms obtained for individual single-crystalline Pd nanoparticles [53, 54, 11], which show an abrupt phase transformation from α to β phase.

5. Solute-induced stacking faults

We proceed to examine the Pd lattice deformation induced by the sharp α/β phase boundary. Specifically, we first explain the formation and dynamics of stacking faults in the spherical particle. Then, we compare with the octahedral and cubic particles to explain the effect of particle shape.

5.1. Stacking faults in the spherical nanoparticle

5.1.1. Formation and spatial distribution

Stacking faults start to form on the surface of the particle at approximately 0.5 s, when the thickness of the β phase shell is approximately 0.5 nm. Figure 8(a) shows the structure of stacking faults at 4.5 s, obtained using the method of common neighbor analysis [55] based on the calculated mean positions of Pd atomic sites. Most of the stacking faults appear in two sets of crystallographically equivalent regions. The

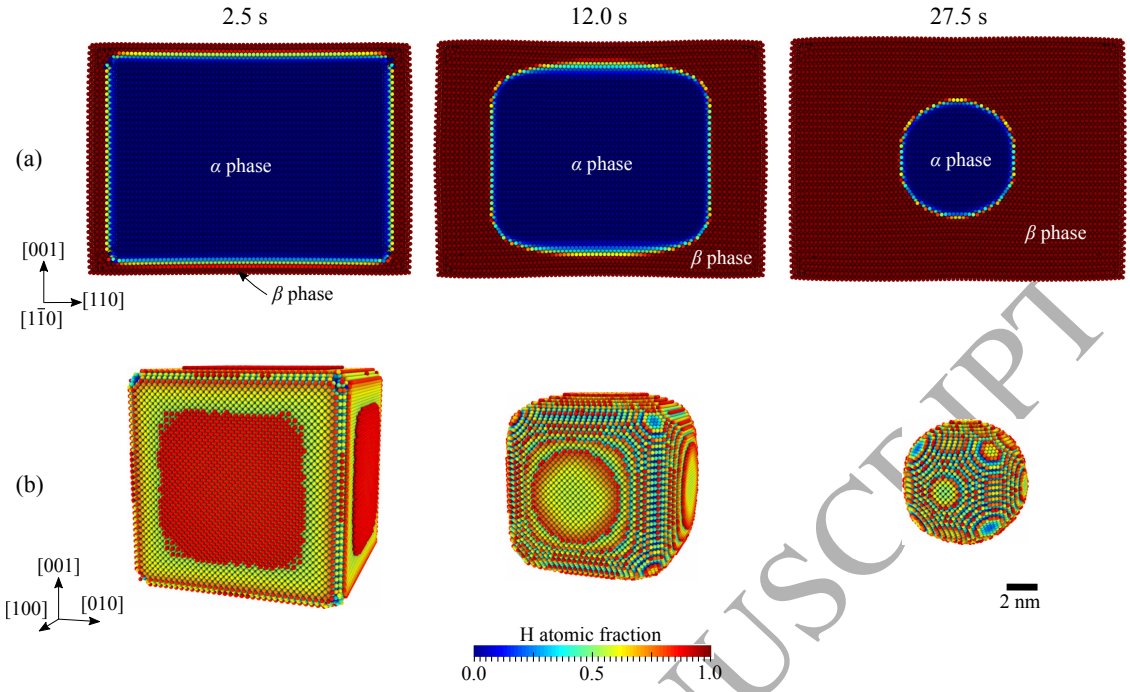

Figure 6: Hydride phase boundary in the cubic particle at three different time instances: (a) H fraction on the middle [1$\bar{1}$0] cross-section, and (b) a perspective view of the extracted phase boundary.

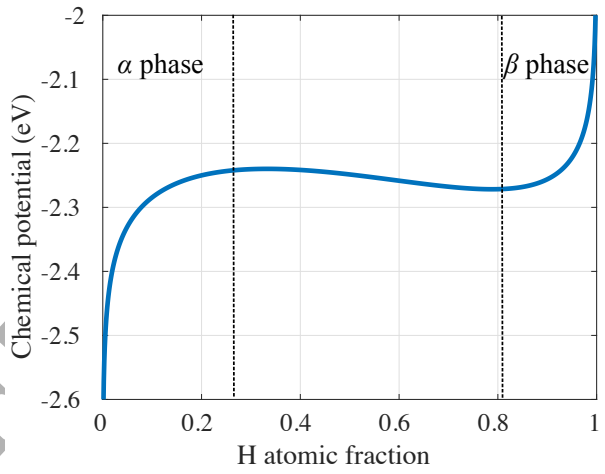

Figure 7: Equilibrium relation between chemical potential and H atomic fraction, calculated using the EAM potential of Zhou *et al.* [48] and the DMD model for bulk Pd-H with a uniform H atomic fraction.

first set, referred to as the ⟨100⟩-centered regions, are spherical sectors with axes in ⟨100⟩ directions and an apex angle of about 40°. The second group, referred to as the ⟨110⟩-centered regions, are spherical sectors with axes in ⟨110⟩ directions and an apex angle of about 50°. In each ⟨100⟩-centered region, four stacking faults are emitted along four different {111} slip planes at 109.5° angle. In each ⟨110⟩-centered region, around twelve stacking faults are emitted along two sets of parallel {111} planes.

To explain the observed distribution pattern, we consider an elastic core-shell model, consisting of a spherical core with radius r_0, elastically matched to a concentric spherical shell whose inner surface has a radius R_0 that is greater than r_0. We set $R_0/r_0 = 1.059$, basing on the lattice expansion of Pd-H from α to β phase. Therefore, the core and the shell are comparable, respectively, with the α phase core and the β

phase shell observed in the DMD simulation. The model equations and the solution process are presented in Appendix A. In particular, after obtaining the equilibrium state, we calculate the resolved shear stress (RSS) on the 12 slip systems of FCC crystals.

Figure 8(b) shows the maximum RSS among all the 12 slip systems, calculated on the core-shell interface using Eq. (A.19). The distribution of maximum RSS is clearly nonuniform. The global maximum value is 3.92 GPa, higher than the critical resolved shear stress (CRSS) of Pd-H[1]. Comparing with the result of the DMD simulation (Fig. 8(a)), we find that the regions where large values of maximum RSS appear coincide with the regions where stacking faults are observed. Moreover, within these regions, the slip system with highest RSS also matches the fault plane of the stacking faults observed in the DMD simulation.

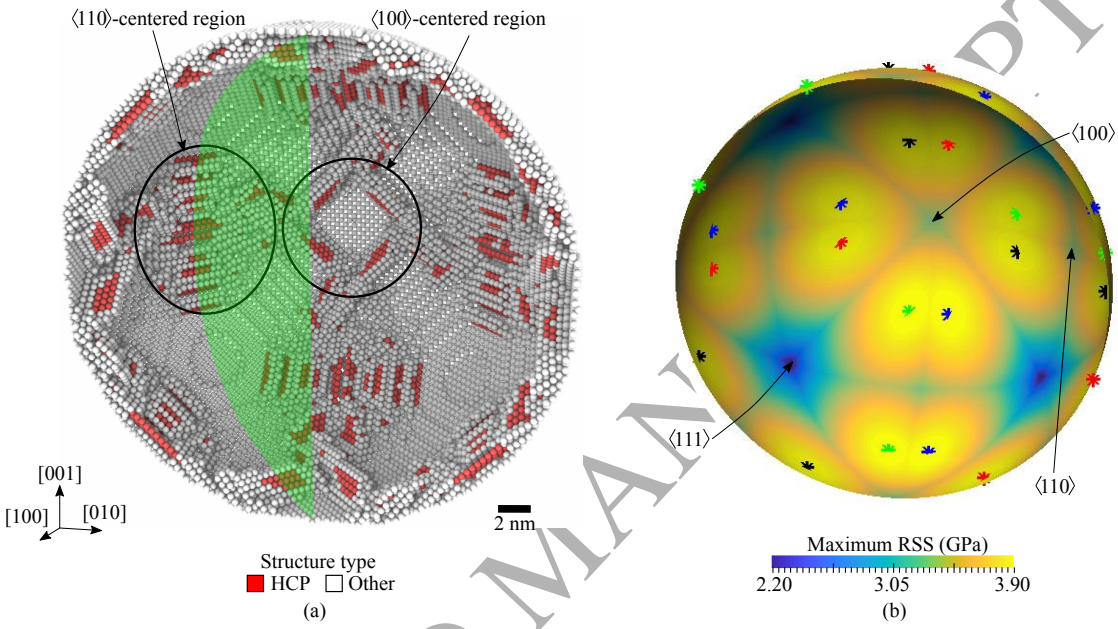

Figure 8: (a) Distribution of stacking faults predicted by the DMD simulation at 4.5 s. (b) Maximum resolved shear stress (RSS) obtained from the core-shell model. In Subfigure (a), the green plane denotes the middle $[1\bar{1}0]$ cross-section. In Subfigure (b), the locations of the global maximum values are marked with asterisks.

For a clearer comparison, Fig. 9 shows the results of both DMD and the core-shell model on the middle $[1\bar{1}0]$ cross-section, i. e., the highlighted plane in Fig. 8(a). From the result of DMD, we find that the stacking faults are emitted on the (111) and $(\bar{1}\bar{1}1)$ slip planes, referred to as slip planes B and C, respectively. All the stacking faults cut through the β phase shell, but do not penetrate the α/β phase boundary. In comparison, Fig. 9(b) shows the maximum RSS among the 3 slip systems associated with these two planes (shown in Table A.1), predicted by the core-shell model. It is clear that the locations of (111) stacking faults coincide with the locations of high RSS associated with (111) plane; and the same agreement holds for the $(\bar{1}\bar{1}1)$ plane. Also, along any radial direction, the maximum RSS associated with both (111) and $(\bar{1}\bar{1}1)$ reaches the highest value at the core-shell interface, then drops immediately to zero inside the α phase.

In summary, the formation of stacking faults in the spherical nanoparticle and the distribution pattern they adopt can be explained as a mechanism for relaxing the residual stress induced by the atomistically sharp α/β phase boundary. The elastic core-shell model is found to be a convenient tool to explain the DMD result. In the next section, we will continue using it, to explain the dynamics (e. g., growth, branching, and disappearance) of the stacking faults caused by the propagation of the α/β phase boundary.

[1]The CRSS of Pd-H is estimated to be between 0.41 GPa and 3.27 GPa, using the embedded atom method (EAM) potential of Zhou *et al.* [48].

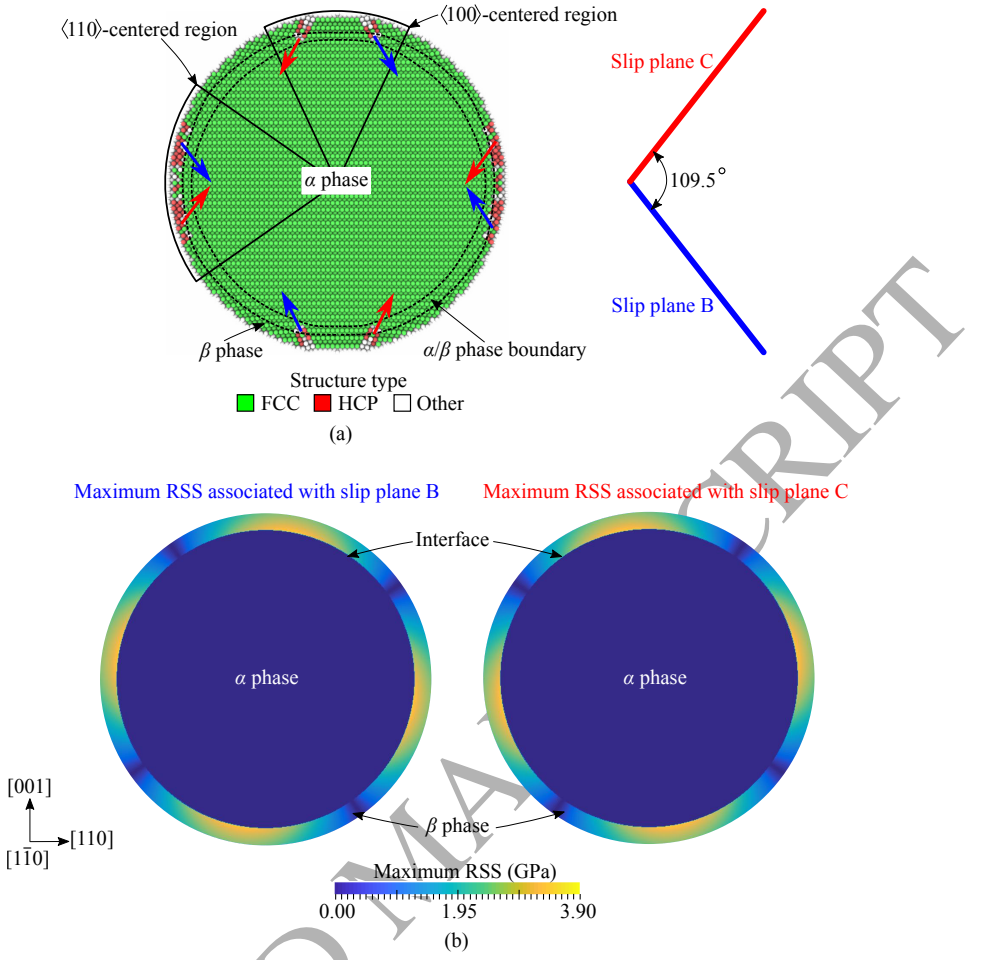

Figure 9: Results of (a) the DMD simulation at 4.5 s and (b) the elastic core-shell model on the middle [1$\bar{1}$0] plane.

5.1.2. Dynamics of stacking faults

We examine the evolution of the stacking faults identified in the previous section. Figure 10 visualizes the evolution of stacking faults in a ⟨100⟩-centered region. Specifically, the images taken at 4.5 s show that as a thin layer of β phase Pd-H develops, four extrinsic stacking faults are emitted from the surface of the particle. Each of them is created by two Shockley partial dislocations on adjacent {111} planes, within the α/β phase boundary. The formation of stacking faults through double Shockley partials has been observed previously in MD simulations of other materials during mechanical deformations (e. g., copper, with relatively low stacking fault energy [56], and aluminum, with relatively high stacking fault energy [57]). Nonetheless, in the present study, the deformation is driven by the transport of solute atoms.

Moreover, Fig. 10 shows that the four stacking faults on different {111} planes form a tunnel-like structure with a 109.5° angle between neighboring walls. A Lomer-Cottrell lock along ⟨110⟩ direction forms at the intersection of each pair of stacking faults. The reaction is

$$1/6[211] + 1/6[\bar{2}1\bar{1}] \rightarrow 1/3[010]. \tag{17}$$

As the α/β phase boundary propagates inwards, the double Shockley partials glide on their {111} slip planes. Because of the sessile Lomer-Cottrell locks, the tunnel-like structure retains its shape, while the four stacking faults extend inwards. At approximately 7.5 s, a new Shockley partial is emitted from the surface of the particle, near each stacking fault. This Shockley partial transforms the extrinsic stacking fault into a three-layer twin.

It is notable that after approximately 17.5 s, the stacking faults stop growing. This can be explained

by the fact that the angle between the fault plane of each stacking fault and the propagation direction of the phase boundary — measured at the tip of the stacking fault and indicated with red and yellow arrows in Fig. 10(b) — gradually increases. At approximately 17.5 s, this angle reaches 90°. After this point, any further extension of the stacking faults would not "catch" the phase boundary and resolve the associated high stress. As a result, the stacking faults stop growing. Later, as the phase boundary moves away from the stacking faults, the tunnel-like stacking fault structure gradually dissolves in the FCC lattice, starting at the surface of the particle.

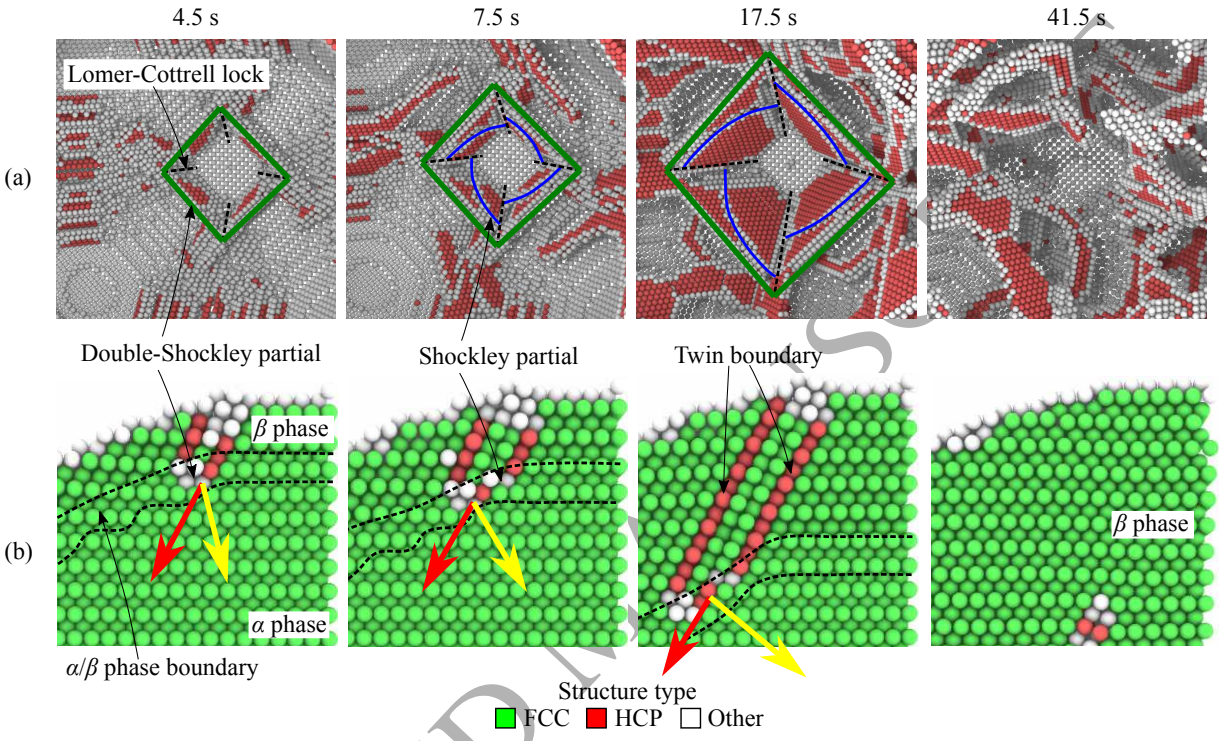

Figure 10: Evolution of stacking faults in a ⟨100⟩-centered region. Subfigure (a) shows a perspective view of the stacking faults. Subfigure (b) shows a middle ⟨110⟩ cross-section of one stacking fault in the tunnel-like structure. The red and yellow arrows indicate the gliding direction of the stacking fault and the propagation direction of the phase boundary, respectively.

Figure 11 visualizes the evolution of stacking faults within a ⟨110⟩-centered region. At around 7.5 s, a stacking fault is emitted from the surface of the particle, gliding on a {111} plane (specifically, slip plane C). This stacking fault is denoted by SF-A for the ease of reference. SF-A is generated by the successive emission of three Shockley partial dislocations from the surface of the particle. The stacking sequences around SF-A are

$$
\begin{aligned}
&(1)\ \cdots\ \mathrm{ABCABCABCABC}\ \cdots,\\
&(2)\ \cdots\ \mathrm{CABC\underline{AC}ABCABC}\ \cdots,\\
&(3)\ \cdots\ \mathrm{BCAB\underline{C}B\underline{A}BCABC}\ \cdots,\\
&(4)\ \cdots\ \mathrm{ABCA\underline{B}AC\underline{B}CABC}\ \cdots,
\end{aligned}
$$

in which the locations of the four stacking sequences are marked in Fig. 11(a). The A-B-C nomenclature denotes the three possible positions of {111} layers in the projection onto a {110} plane. The underlined letters indicate the planes in a local hexagonal close-packed (HCP) stacking sequence. Therefore, the four regions have the features of: (1) a perfect FCC lattice, (2) an intrinsic stacking fault, (3) an extrinsic stacking fault, and (4) a three-layer twin, respectively. This type of stacking fault structure has been observed previously in MD simulations of mechanical twinning (e. g., in aluminum [57] and steel [58]). Nonetheless, our results reveal that, this twinning process can also be driven by the high residual stress due to phase transformation in chemical reactions (specifically, hydrogenation of Pd).

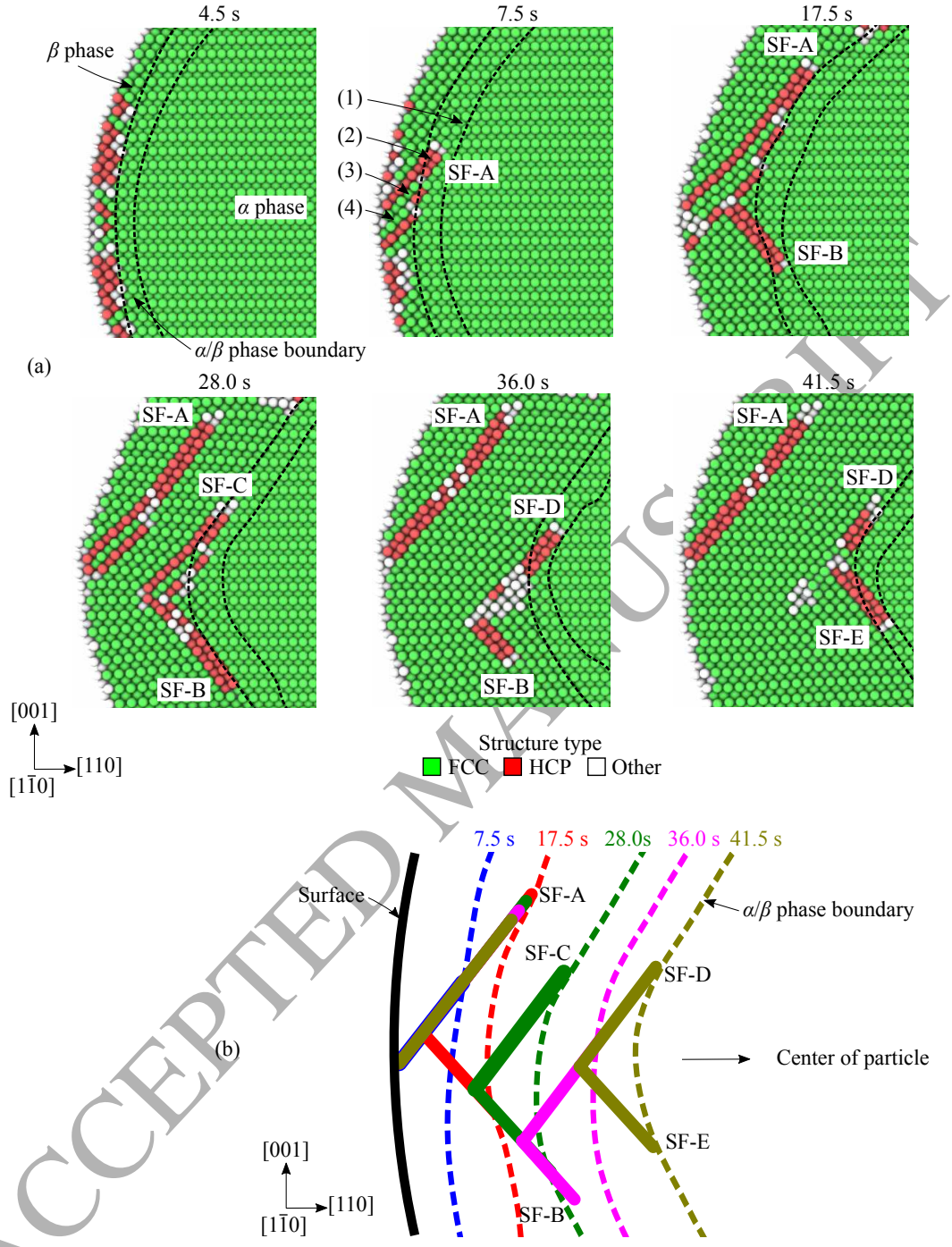

Figure 11: Time evolution of stacking faults in a ⟨110⟩-centered region. (a) Solution snapshots at six time instances. (The middle [1$\bar{1}$0] cross-section is shown.) (b) Superposition of the stacking faults at the six time instances.

As the α/β phase boundary propagates towards the center of the particle, the Shockley partials glide along their slip planes, which drives SF-A to extend. SF-A keeps in connection with both the surface of the particle and the phase boundary, until approximately 17.5 s, when the fault plane becomes tangent to the phase boundary. Similar to the ⟨100⟩-centered region, after this point of time, SF-A stops growing. However, it is notable that a new intrinsic stacking fault is emitted from SF-A on slip plane B. This new stacking fault

is denoted by SF-B in Fig. 11(a). The tip of SF-B is within the phase boundary. Also, a Lomer-Cottrell lock forms at the intersection of SF-A and SF-B.

We employ the core-shell model to understand the emission of SF-B from SF-A. Figure 12 shows that at 17.5 s, the tip of SF-A has just passed a region of high RSS associated with slip plane B. It is likely that this region of high RSS caused the emission of SF-B. Figure 12 also shows that the RSS associated with slip plane B near the stacking fault on a different slip plane is smaller in the ⟨100⟩-centered regions than in the ⟨110⟩-centered regions. This explains why the same phenomenon does not occur in the ⟨100⟩-centered regions.

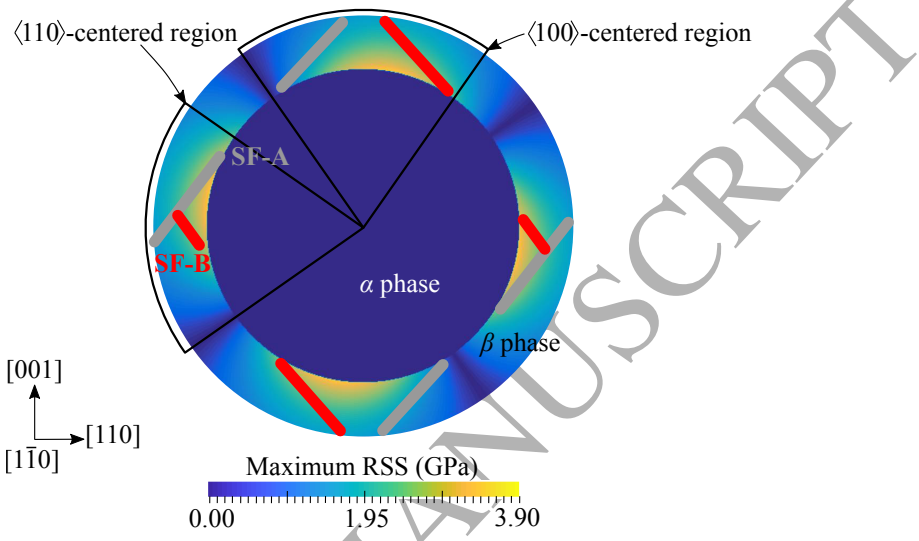

Figure 12: Superposition of the field of maximum RSS associated with slip plane B, predicted by the core-shell model, with stacking faults observed at 17.5 s. Stacking faults on slip plane B are colored in red.

As the phase boundary propagates inwards, the Shockley partial associated with SF-B glides on its slip plane (see Fig. 11(a)). At approximately 28.0 s, it is disconnected from SF-A. At the same time, a detwinning process takes place in SF-A, by the gliding of Shockley partials away from the phase boundary. Also, a new stacking fault, denoted by SF-C, has been emitted from SF-B with a Lomer-Cottrell lock at their intersection. The same phenomenon occurs repeatedly until approximately 53.0 s, when the surface area of the phase boundary is considerably small and the elastic lattice deformation alone is enough to release the residual stress on the interface. Overall, the dynamics of stacking faults in the ⟨110⟩-centered regions is dominated by the emission of new stacking faults from existing ones, the gliding of stacking faults towards the phase boundary, and the annihilation of stacking faults as the phase boundary moves away. This mechanism is schematically illustrated in Fig. 11(b).

In summary, the stacking faults observed during the H absorption process are on {111} planes, which is typical for FCC crystals. After a thin layer of β phase Pd-H has formed under the surface of the particle, stacking faults start to appear within the β phase, mostly in ⟨100⟩- and ⟨110⟩-centered regions, where the RSS on {111} planes is high. The {111} fault planes of these stacking faults do not pass through the center of the particle. As a result, after some time, they become tangent to the phase boundary. When this happens, the stacking faults stop growing, as the RSS at the tips significantly decreases. In the ⟨110⟩-centered regions, we observe the emission of new stacking faults from old ones, as a mechanism to "catch" the movement of the phase boundary. This phenomenon does not appear in the ⟨100⟩-centered regions. The reason is that in the ⟨100⟩-centered regions, the maximum RSS near existing stacking faults associated with different slip planes is relatively small and cannot drive the emission of new stacking faults.

Recent experimental studies [16, 14] have revealed that the hydride phase transformation in Pd nanoparticles is driven by the propagation of a sharp α/β phase boundary. Attendant to the α/β phase transformation, there is a lattice expansion with approximately 10.4% increase in volume. Therefore, near the phase boundary, there is either elastic or plastic deformation of Pd lattice in order to release such lattice mismatch. In

this regard, our DMD simulations have predicted the formation and dynamics of stacking faults under the spherical-shell mechanism of the morphological evolution of the hydride phase boundary. However, it should be noted again that the DMD model does not explicitly resolve the thermal vibrations of atoms, and is a statistical model in nature to simulate long-term processes. Therefore, it cannot directly capture the effects of *random* thermal vibrations.

5.2. Effect of particle shape

Next, we examine the octahedral particle which, in contrast to the sphere, has planar faces and sharp edges and corners. Figure 13 shows the initial distribution of stacking faults at 4.5 s. The distribution pattern is different from that in the spherical particle. Specifically, stacking faults are formed near the edges of the particle, forming 12 separate, fusiform branches. In each branch, two stacking faults are emitted along two different {111} slip planes. This distribution pattern is due to the fact that after the formation of a thin β phase layer, the edges of the particle have relatively large displacements parallel to {111} planes.

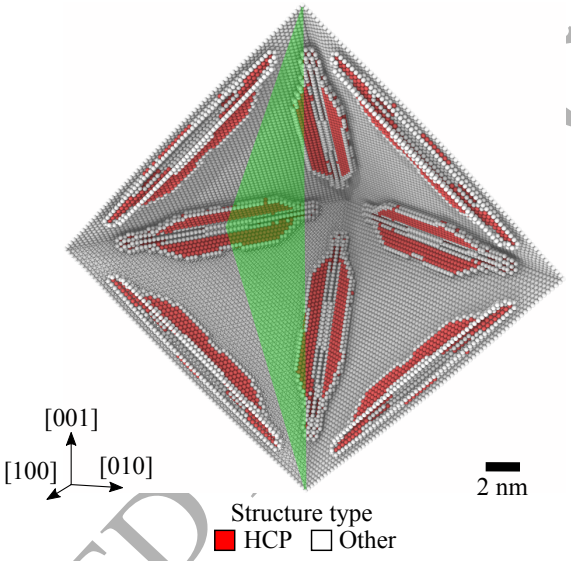

Figure 13: Distribution of stacking faults predicted by the DMD simulation at 4.5 s. The green plane denotes the middle $[1\bar{1}0]$ cross-section.

Figure 14 visualizes the evolution of the stacking faults by showing the structure type on the middle $[1\bar{1}0]$ cross-section (i. e., the highlighted plane in Fig. 13). At 4.5 s, the zoom-in view shows that the three outermost {111} layers in the β phase undergo a shear displacement, due to the lattice expansion from α to β phase. The stacking faults keep in connection with the surface of the particle. They separate a small region from the FCC matrix, in which the Pd lattice is largely distorted. Moreover, the edges of the octahedron stretch outwards, forming a star-like shape. The stretching is caused by the interaction of expanded neighboring faces. This star-shaped deformation has also been observed experimentally in Pd nanocubes with edge length of approximately 60 nm [14]. As the phase boundary propagates, the stacking faults move towards the center of the particle. At 23.0 s, an intersection of twins takes place outside the octahedral edges of the phase boundary, separating a rhomboid FCC block from the FCC matrix. As the phase boundary approaches the center of the particle, the size of the stacking faults reduces, and they become disconnected from the surface of the particle.

Next, we examine in detail the dynamics of the observed stacking faults. We focus on the stacking faults near one edge of the particle, and the result is shown in Fig. 15. At 4.5 s, two Shockley partials are emitted from the distorted region, leaving behind two intrinsic stacking faults. We focus on one of the two stacking faults, and the associated partial dislocation is denoted by PD-A for the ease of reference. At 7.0 s, a new Shockley partial, denoted by PD-B, has been emitted within the phase boundary, adjacent to the previously formed stacking fault. PD-B glides away from the distorted region, transforming the intrinsic stacking fault to an extrinsic one. By contrast, PD-A glides in the opposite direction, because it is away from the phase

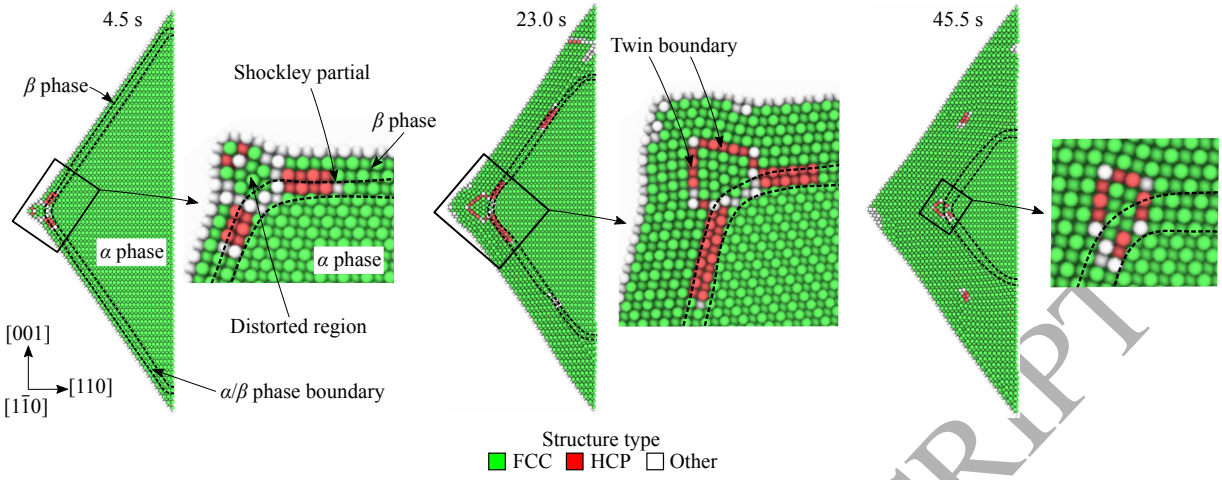

Figure 14: Evolution of stacking faults in the octahedral particle.

boundary. As the phase boundary propagates inwards, PD-B keeps growing, and PD-A gradually disappears. As a result, the stacking fault moves over one atomic layer in the direction perpendicular to its fault plane. The same layer-by-layer process is repeated until approximately 56.5 s, when the surface area of the phase boundary is considerably small.

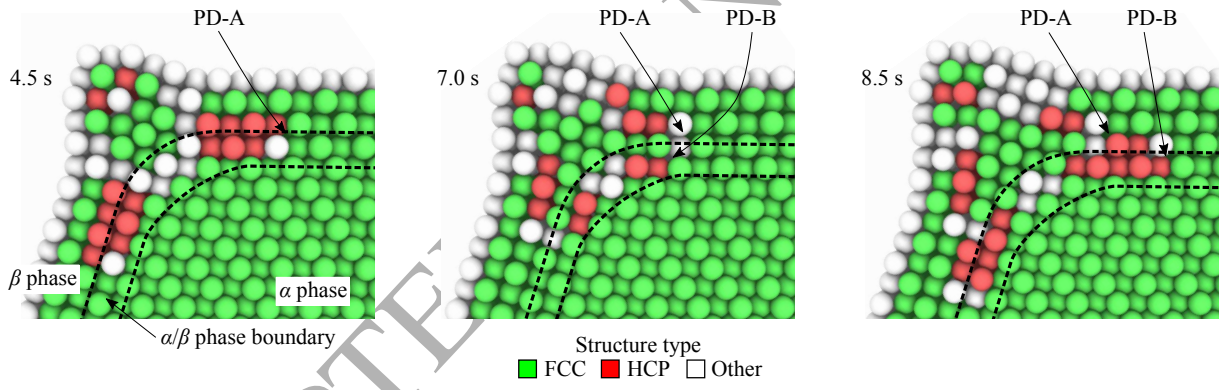

Figure 15: Details of the dynamics of the stacking faults in the octahedral particle.

Notably, in the octahedral particle, the dynamics of the stacking faults is dominated by the movement of partial dislocations on consecutive fault planes. This mechanism, clearly different from that in the spherical particle, is dominated by the morphology of the phase boundary. In the octahedral particle, the phase boundary retains planar {111} faces during the H absorption process, and stacking faults start to appear near the edges of the phase boundary. Therefore, as the phase boundary moves, the stacking faults quickly become tangent to it. When this happens, the stacking faults stop gliding, and new partial dislocations have been emitted from the edges of the phase boundary. These dislocations are adjacent to the existing stacking faults, driving them to "catch" the phase boundary.

Moreover, our DMD results show that in both the spherical and octahedral Pd particles, the propagation of the atomistically sharp phase boundary results in the formation, and then the *removal* of crystallographic imperfections (specifically, stacking faults). The ability of nanostructured Pd to "self-heal" defects during H loading and unloading processes has been discovered in a few recent experimental studies [16, 59]. To this end, our simulations have provided additional, atomic-level details on the dynamics of stacking faults during the H absorption process.

By contrast, in the cubic particle, no stacking faults appear during the H absorption process. In order to explain this difference, we examine the area on one {111} plane that is mismatched with another parallel

{111} plane. In this regard, Fig. 16 schematically compares the three particles in different shape. Two parallel {111} atomic layers are sketched: one in the β phase and the other cutting the phase boundary. The misfit area is colored in blue. Compared to the sphere and the octahedron, the cubic particle has a much smaller misfit area. Since the {111} family of planes is the major operative slip plane in the FCC crystal, the large misfit area in the spherical and octahedral particles leads to large lateral movement between two {111} layers and hence the emergence of stacking faults. On the other hand, the smaller misfit area in the cubic particle explains the absence of stacking fault.

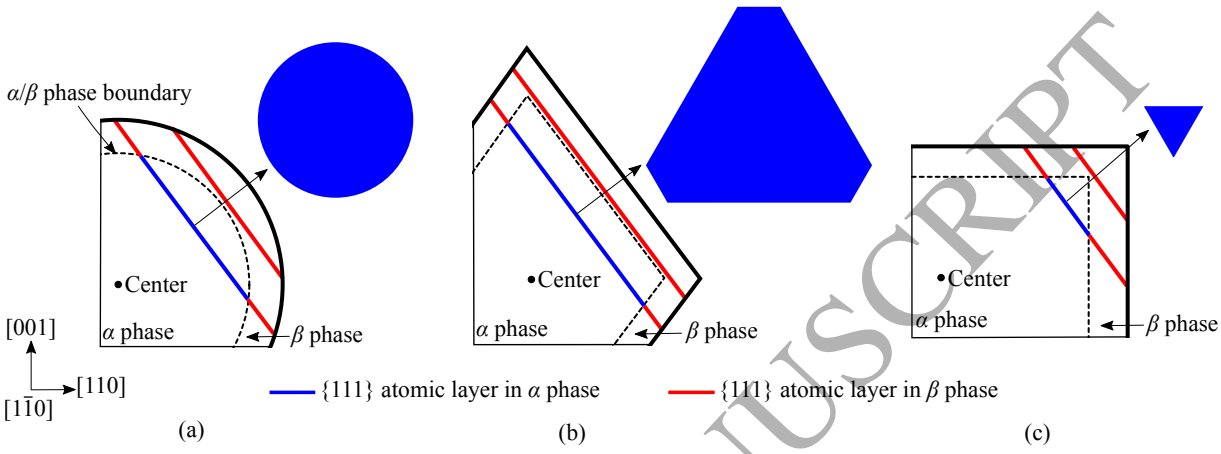

Figure 16: Schematic illustration of the effect of particle shape on the lattice deformation: (a) spherical, (b) octahedral, and (c) cubic particles.

6. Rate of hydrogen absorption

We proceed to examine the effect of particle shape on the overall H absorption process. Figure 17 shows the time-history of H concentration in each particle and its time derivative. Notably, the cubic particle absorbs H faster than the other two. This can be explained by two factors. First, the three particles are designed to have approximately the same volume. Under this condition, the cubic particle has the highest surface-area-to-volume ratio. Therefore, during the early stage when a thin layer of β phase is formed, the phase boundary in the cubic particle provides largest surface area for H diffusion into the α phase core. Second, the phase boundary in the cubic particle remains coherent, which may facilitate the absorption of H as explained in Section 4.

Moreover, Fig. 17(b) shows that from approximately 4.5 s to 16.5 s, the rate of H absorption in the octahedral particle is clearly lower than that in the spherical one. This difference cannot be explained through the comparison of surface-area-to-volume ratio. In fact, for the same volume, the surface-area-to-volume ratio of an octahedron is higher than that of a sphere. Instead, the difference may be related to the volume fraction of solute-induced stacking faults. Figure 18 shows that during the aforementioned time period, the octahedral particle has a higher volume fraction of stacking faults than the spherical one. In other words, the phase boundary in the octahedral particle has a larger semi-coherent area. Therefore, in this stage, misfit dislocations become an important factor that controls the rate of H absorption, overriding the effect of surface-area-to-volume ratio.

7. Comparison with Molecular Dynamics simulation

The main advantage of DMD over Molecular Dynamics (MD) is the ability to simulate processes with much longer time scales while maintaining the atomistic spatial resolution. This advantage is achieved by modeling thermal vibrations through a probabilistic approach, instead of resolving them. Therefore, it is both interesting and useful to compare the result of DMD with that of MD. It is impossible to simulate the entire H absorption process using MD due to the small time-step size (less than 1 fs). Here, we initialize an

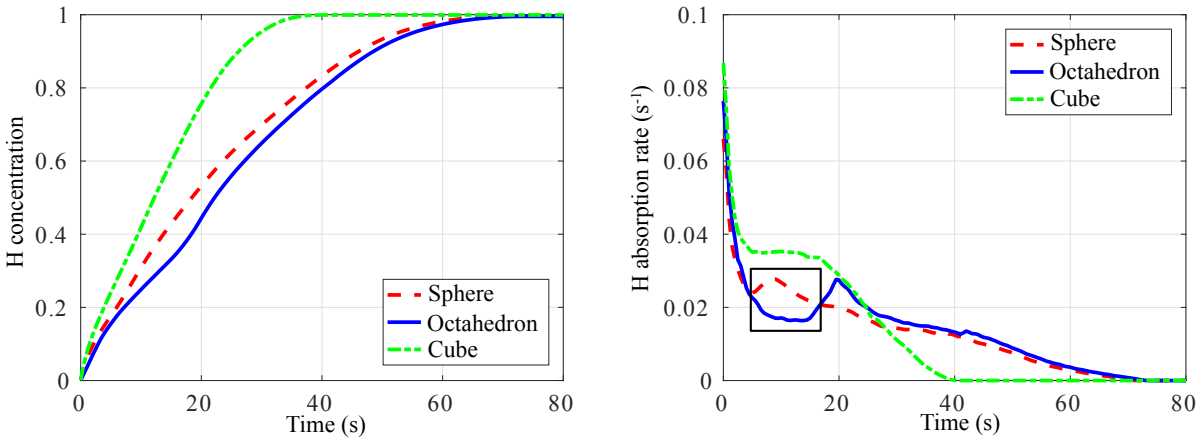

(a) (b)

Figure 17: Time-history of H absorption: (a) H concentration and (b) rate of H absorption.

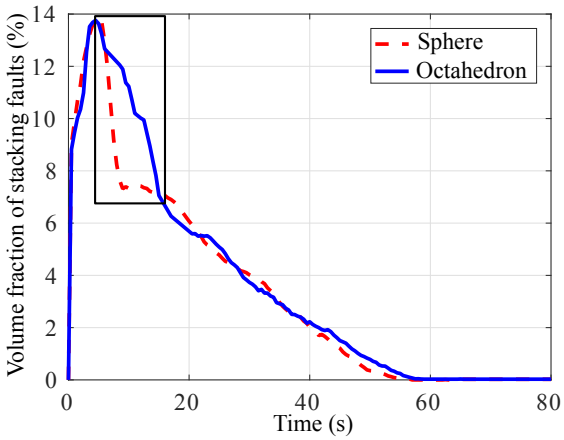

Figure 18: Time-history of volume fraction of stacking faults.

MD simulation using an intermediate DMD solution that exhibits both a sharp phase boundary and misfit dislocations. We run the MD simulation for a short period of time (1.0 ns), during which the DMD result remains almost unchanged. Through this experiment, we attempt to verify that the key features predicted by DMD are indeed energetically stable.

Specifically, we use the DMD result (i. e., $\{\bar{\boldsymbol{q}}\}$, $\{\sigma\}$ and $\{x\}$) at 17.5 s for the spherical particle to initialize the MD simulation. Based on the trial Hamiltonian in Eq. (6), it can be shown that in the DMD method, the instantaneous position of each site and the occupancy of each interstitial site follow the normal and Bernoulli distributions, respectively. Therefore, for the sake of comparison, the initial positions of Pd atoms in the MD simulation are generated according to the normal distributions with mean $\{\bar{\boldsymbol{q}}\}$ and standard deviation $\{\sigma\}$. The initial occupancies of interstitial sites are generated according to the Bernoulli distributions with mean $\{x\}$ (i. e., atomic fractions). If an interstitial site is occupied, the initial position of the H atom is generated according to the corresponding normal distribution. As a result, initially there are $261,563$ Pd atoms and $138,871$ H atoms in the MD simulation.

The MD simulation is performed using the Large-scale Atomic/Molecular Massively Parallel Simulator (LAMMPS) program [60]. We employ the embedded atom method (EAM) potential developed by Zhou *et al.* [48], which is the same as the one used in the DMD simulation. The temperature is set to 300 K using

a Nosé-Hoover thermostat. The integration time-step size is 0.1 fs, and the total simulation time is 1.0 ns. Within this small time window, the H concentration in the particle is almost unchanged. Therefore, the total numbers of both Pd and H atoms are kept constant throughout the MD simulation. The time-averaged atomic positions of Pd atoms over 0.01 ns are calculated and used to identify lattice structure types, in order to mitigate the large perturbations of Pd atomic positions in the β phase caused by the existence of H atoms.

Figure 19 shows comparisons of phase boundary and stacking faults between MD and DMD simulations. Notably, the MD simulation reveals that during the time period of 1.0 ns, the equilibrium positions of most Pd and H atoms only vary slightly, despite the continuous atomic vibrations. As a result, both the phase boundary and the stacking faults still exist and are in the same places during this short time period. Their positions coincide with those obtained from the DMD simulation. Therefore, the DMD method has provided an energetically stable configuration of Pd and H atoms. Moreover, a perspective view of the distribution of H atoms in the MD simulation is shown in Fig. 20, which further indicates the separation of α and β phases during the 1.0 ns. However, the MD method is not able to predict the slow motion of the phase boundary and hence the dynamics of the induced stacking faults, due to its extremely short simulation time window. By contrast, the DMD results presented in the previous sections have provided the atomic-level details involved in the entire diffusion-deformation coupled process.

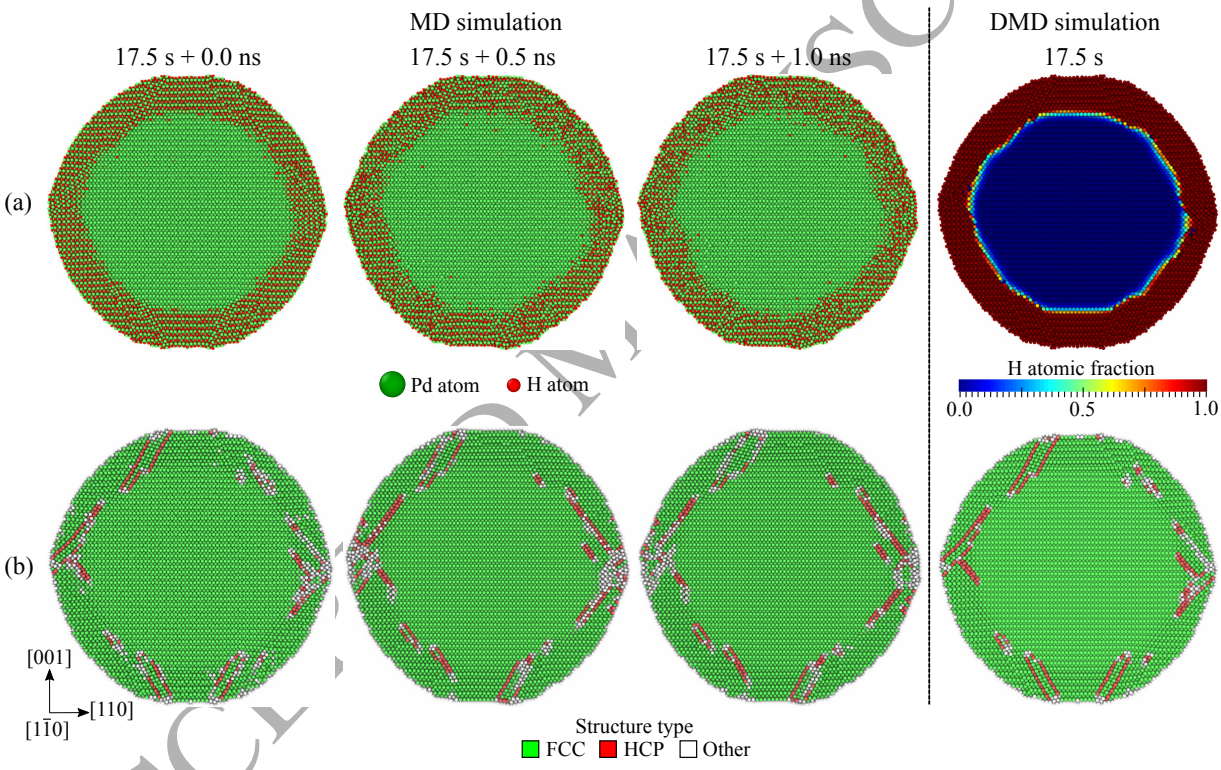

Figure 19: Comparisons between MD and DMD simulations: (a) phase boundary, and (b) stacking faults.

8. Conclusions

We have analyzed the absorption of hydrogen (H) by three palladium (Pd) nanoparticles of different morphologies (i. e., spherical, octahedral and cubic) using Diffusive Molecular Dynamics (DMD). The chief advantage of DMD which renders it ideally suited for this application is its ability to simulate long-term behavior of atomic systems without the time constraints inherent to Molecular Dynamics (MD). Indeed, atomic resolution is required in order to ascertain the complex mechanisms set in motion by H absorption into the Pd nanoparticles. These mechanisms, as identified in calculations, include phase transformation,

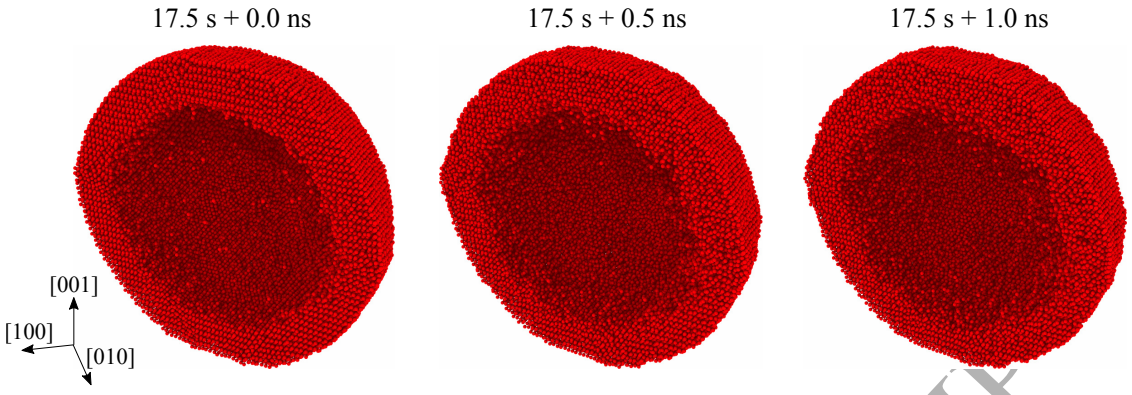

Figure 20: Spatial distribution of H atoms at three different time instances in the MD simulation.

phase boundary motion, misfit dislocations, stacking faults and their evolution. The motion of the α/β phase boundary is the net result of a complex interplay between these mechanisms.

Several main findings afforded by the calculations are noteworthy. Firstly, the hydride phase transformation in Pd nanoparticles is dominated by the propagation of an atomistically sharp α/β phase boundary. The phase boundary in the cubic particle remains coherent during the H absorption process, whereas stacking faults are observed in the spherical and octahedral particles. These stacking faults move together with the propagating sharp phase boundary in order to release the elastic stress induced at the phase boundary by the misfit between the α and β lattices. Specifically, in the spherical particle, the movement of stacking faults is dominated by the emission of a new stacking fault from an existing one, the gliding of stacking faults together with the phase boundary and the annihilation of stacking faults behind from the phase boundary. In the octahedral particle, the dynamics of stacking faults is dominated by the movement of partial dislocations on consecutive fault planes. Moreover, the particle shape has an effect on the diffusion of H. Specifically, the cubic particle exhibits the ability to absorb H atoms faster than the other two shapes. Our DMD model also predicts that the formation and movement of stacking faults may slow down the propagation of the hydride phase boundary, and hence reduce the speed of H absorption. In this regard, the two-way interaction between H absorption and lattice deformation is remarkable.

These predictions also indicate that for the particle size and shapes under consideration, the cubic particle aligned with {100} planes may be optimal for H storage applications. The suppression of stacking fault formation in the cubic nanoparticles and the persistent coherence of the phase boundary may also be expected to enhance the repeatability of the storage cycle and, therefore, the useful life of the nanoparticles. However, the mechanisms of phase boundary motion and the H storage characteristics identified in this study are likely to be size dependent. In particular, the coherence of the phase boundary may be lost for cubic nanoparticles exceeding a critical size. Larger nanoparticle sizes also promote decomposition into grains separated by grain boundaries. Under those conditions, grain boundaries are known to mediate hydrogenation and to influence the storage characteristics of individual nanoparticles [61]. These and other trade-offs suggest themselves as worthwhile directions for further study.

Acknowledgments

The authors gratefully acknowledge the support of the U. S. Office of Naval Research (ONR) under grant number N00014-17-1-2831, the Ministerio de Economía y Competitividad of Spain under grant number DPI2015-66534-R, and the U. S. Army Research Laboratory (ARL) through the Materials in Extreme Dynamic Environments (MEDE) Collaborative Research Alliance (CRA) under Award Number W911NF-11-R-0001.

Appendix A. An elastic core-shell model

The elastic field of a spherical core in an elastically matched, concentric spherical shell can be obtained by elementary methods of linear elasticity. For completeness, here we present a short derivation for the case

of isotropic elasticity with Lamé constants $\lambda^{(s)}$ and $\mu^{(s)}$ for the shell and $\lambda^{(c)}$ and $\mu^{(c)}$ for the core. The shell undergoes a volumetric expansion $\kappa = \Delta V/V$, i. e., its volume V would increase by $\Delta V = \kappa V$ if the core were released from the shell. We employ spherically symmetric displacements in the spherical coordinate system (r, θ, ϕ)

$$u_r = u_r(r), \tag{A.1}$$

where r refers to the radial distance. The corresponding strains are

$$\epsilon_{rr} = \frac{du_r}{dr}, \qquad \epsilon_{tt} = \frac{u_r}{r}, \tag{A.2}$$

where t refers to any coordinate (i. e., polar angle θ or azimuthal angle ϕ) that has transverse direction perpendicular to the radial direction. From Hooke's law, the stresses follow as

$$\sigma_{rr} = \lambda(\epsilon_{rr} + 2\epsilon_{tt}) + 2\mu\epsilon_{rr}, \tag{A.3a}$$
$$\sigma_{tt} = \lambda(\epsilon_{rr} + 2\epsilon_{tt}) + 2\mu\epsilon_{tt}. \tag{A.3b}$$

The radial equilibrium equation is

$$\frac{d\sigma_{rr}}{dr} + 2\frac{\sigma_{rr} - \sigma_{tt}}{r} = 0, \tag{A.4}$$

or, in terms of displacements,

$$\frac{d^2u_r}{dr^2} + \frac{2}{r}\frac{du_r}{dr} - \frac{2u_r}{r^2} = 0. \tag{A.5}$$

The corresponding general solution is

$$u_r = Ar + \frac{B}{r^2}, \tag{A.6}$$

with stresses

$$\sigma_{rr} = 3\lambda A + 2\mu\left(A - \frac{2B}{r^3}\right), \tag{A.7a}$$
$$\sigma_{tt} = 3\lambda A + 2\mu\left(A + \frac{B}{r^3}\right). \tag{A.7b}$$

If the core were released from the shell, the change of volume in the shell would induce a displacement at its inner boundary such that

$$4\pi {R^{(c)}}^2 u_0 = \kappa\frac{4\pi {R^{(c)}}^3}{3}, \tag{A.8}$$

or

$$u_0 = \frac{\kappa}{3}R^{(c)}, \tag{A.9}$$

where $R^{(c)}$ is the radius of the core. The core-shell system then undergoes displacements

$$u_r^{(c)} = A^{(c)}r + \frac{B^{(c)}}{r^2}, \quad r < R^{(c)}, \tag{A.10a}$$
$$u_r^{(s)} = A^{(s)}r + \frac{B^{(s)}}{r^2}, \quad r > R^{(c)}, \tag{A.10b}$$

in order to restore compatibility. The corresponding boundary conditions are

$$u_r^{(c)}(0) < +\infty, \tag{A.11a}$$
$$u_r^{(c)}(R^{(c)}) = u_0 + u_r^{(s)}(R^{(c)}), \tag{A.11b}$$
$$\sigma_{rr}^{(c)}(R^{(c)}) = \sigma_{rr}^{(s)}(R^{(c)}), \tag{A.11c}$$
$$\sigma_{rr}^{(s)}(R^{(s)}) = 0, \tag{A.11d}$$

where $R^{(s)}$ is the radius of the outer surface of the shell. Solving for the constants, we find $B^{(c)} = 0$ and

$$A^{(c)} = \frac{4\mu^{(s)}\kappa(3\lambda^{(s)} + 2\mu^{(s)})\left({R^{(c)}}^3 - {R^{(s)}}^3\right)}{D}, \tag{A.12a}$$

$$A^{(s)} = \frac{4\mu^{(s)}{R^{(c)}}^3\kappa(3\lambda^{(c)} + 2\mu^{(c)})}{D}, \tag{A.12b}$$

$$B^{(s)} = \frac{{R^{(c)}}^3{R^{(s)}}^3\kappa(3\lambda^{(c)} + 2\mu^{(c)})(3\lambda^{(s)} + 2\mu^{(s)})}{D}, \tag{A.12c}$$

with

$$\begin{aligned} D = &-12\mu^{(s)}{R^{(c)}}^3(3\lambda^{(c)} - 3\lambda^{(s)} + 2\mu^{(c)} - 2\mu^{(s)}) \\ &- 3{R^{(s)}}^3(3\lambda^{(s)} + 2\mu^{(s)})(3\lambda^{(c)} + 2\mu^{(c)} + 4\mu^{(s)}). \end{aligned} \tag{A.13}$$

By spherical symmetry, the stress tensor has the representation

$$\boldsymbol{\sigma} = \sigma_{rr}\boldsymbol{e}_r \otimes \boldsymbol{e}_r + \sigma_{tt}(\boldsymbol{I} - \boldsymbol{e}_r \otimes \boldsymbol{e}_r), \tag{A.14}$$

where $\boldsymbol{e}_r$ is radial unit vector, $\otimes$ is the dyadic product and $\boldsymbol{I}$ is the identity matrix. In an FCC crystal, the slip systems based on Schmid and Boas' nomenclature are summarized in Table A.1. The corresponding resolved shear stress (RSS) in a slip system n of slip plane $\boldsymbol{m}$ and slip direction $\boldsymbol{s}$ is

$$\tau(r, \theta, \phi; n) = \boldsymbol{s}^T\boldsymbol{\sigma}\boldsymbol{m} = (\boldsymbol{e}_r \cdot \boldsymbol{s})(\boldsymbol{e}_r \cdot \boldsymbol{m})(\sigma_{rr} - \sigma_{tt}) \equiv s_r m_r T(r), \tag{A.15}$$

where $s_r m_r$ is the Schmidt factor. On the interface $r = R^{(c)}$ in the shell, from the elastic stress field we compute

$$T(R^{(c)}) \equiv \sigma_{rr} - \sigma_{tt} = -\frac{6\mu^{(s)}{R^{(s)}}^3\kappa(3\lambda^{(c)} + 2\mu^{(c)})(3\lambda^{(s)} + 2\mu^{(s)})}{D}. \tag{A.16}$$

A straightforward calculation shows that the corresponding global maximum value of τ on the interface $r = R^{(c)}$ is

$$\tau_{\max} = \max_{\theta,\phi} |\tau(R^{(c)}, \theta, \phi; n)| = \frac{1}{2}|T(R^{(c)})|, \tag{A.17}$$

which is the same for all the slip systems. The maximum RSS is attained at the interfacial points corresponding to

$$\boldsymbol{e}_r = \frac{\sqrt{2}}{2}(\boldsymbol{m} \pm \boldsymbol{s}), \tag{A.18a}$$

$$\boldsymbol{e}_r = -\frac{\sqrt{2}}{2}(\boldsymbol{m} \pm \boldsymbol{s}). \tag{A.18b}$$

The maximum value of RSS at the position (r, θ, ϕ) among a group of selected slip systems is

$$\bar{\tau}(r, \theta, \phi) = \max_{n} |\tau(r, \theta, \phi; n)|. \tag{A.19}$$

In comparison with the DMD simulations for the Pd-H system, we consider the volumetric expansion of the shell induced by the α/β hydride phase transformation. Therefore, the volumetric expansion ratio is

$$\kappa = 3\frac{a_\beta - a_\alpha}{a_\alpha} \tag{A.20}$$

where a_α and a_β denote the lattice constants of α and β phase, respectively. The structural and elastic properties used in the core-shell model are summarized in Table A.2.

Slip system n	A2	A3	A6	B2	B4	B5
$\sqrt{2}\boldsymbol{s}$	$[01\bar{1}]$	$[101]$	$[\bar{1}\bar{1}0]$	$[0\bar{1}1]$	$[10\bar{1}]$	$[\bar{1}10]$
$\sqrt{3}\boldsymbol{m}$	$(\bar{1}11)$	$(\bar{1}11)$	$(\bar{1}11)$	(111)	(111)	(111)
Slip system n	C1	C3	C5	D1	D4	D6
$\sqrt{2}\boldsymbol{s}$	$[011]$	$[\bar{1}0\bar{1}]$	$[1\bar{1}0]$	$[0\bar{1}\bar{1}]$	$[\bar{1}01]$	$[110]$
$\sqrt{3}\boldsymbol{m}$	$(\bar{1}\bar{1}1)$	$(\bar{1}\bar{1}1)$	$(\bar{1}\bar{1}1)$	$(1\bar{1}1)$	$(1\bar{1}1)$	$(1\bar{1}1)$

Table A.1: Slip-system sets in Schmid and Boas' nomenclature for the FCC crystal class. The vector $\boldsymbol{m}$ is the unit normal to the slip plane, and $\boldsymbol{s}$ is the unit vector in the direction of the Burgers vector. All vectors are expressed in the cartesian coordinate system.

	Core (α phase)	Shell (β phase)	Source
Lattice constant a (Å)	3.885	4.115	From the DMD simulations
Elastic constant C_{11} (GPa)	245.8	241.7	From Pd and PdH_1 in
Elastic constant C_{12} (GPa)	199.8	190.3	Ref. [48], respectively

Table A.2: Compilation of material constants for α and β phase Pd-H.

References

[1] D. A. Cogswell, M. Z. Bazant, Theory of coherent nucleation in phase-separating nanoparticles, Nano Letters 13 (7) (2013) 3036–3041.

[2] X. Zhang, M. van Hulzen, D. P. Singh, A. Brownrigg, J. P. Wright, N. H. van Dijk, M. Wagemaker, Rate-induced solubility and suppression of the first-order phase transition in olivine lifepo4, Nano Letters 14 (5) (2014) 2279–2285.

[3] B. Sakintuna, F. Lamari-Darkrim, M. Hirscher, Metal hydride materials for solid hydrogen storage: a review, International Journal of Hydrogen Energy 32 (9) (2007) 1121–1140.

[4] D. Mori, K. Hirose, Recent challenges of hydrogen storage technologies for fuel cell vehicles, International Journal of Hydrogen Energy 34 (10) (2009) 4569–4574.

[5] D. Chartouni, N. Kuriyama, T. Kiyobayashi, J. Chen, Metal hydride fuel cell with intrinsic capacity, International Journal of Hydrogen Energy 27 (9) (2002) 945–952.

[6] A. Pundt, Hydrogen in nano-sized metals, Advanced Engineering Materials 6 (1-2) (2004) 11–21.

[7] M. Yamauchi, R. Ikeda, H. Kitagawa, M. Takata, Nanosize effects on hydrogen storage in palladium, The Journal of Physical Chemistry C 112 (9) (2008) 3294–3299.

[8] R. Griessen, N. Strohfeldt, H. Giessen, Thermodynamics of the hybrid interaction of hydrogen with palladium nanoparticles, Nature Materials 15 (3) (2016) 311.

[9] B. D. Adams, A. Chen, The role of palladium in a hydrogen economy, Materials Today 14 (6) (2011) 282–289.

[10] R. Bardhan, L. O. Hedges, C. L. Pint, A. Javey, S. Whitelam, J. J. Urban, Uncovering the intrinsic size dependence of hydriding phase transformations in nanocrystals, Nature Materials 12 (10) (2013) 905–912.

[11] A. Baldi, T. C. Narayan, A. L. Koh, J. A. Dionne, In situ detection of hydrogen-induced phase transitions in individual palladium nanocrystals, Nature Materials 13 (12) (2014) 1143–1148.

[12] G. Li, H. Kobayashi, S. Dekura, R. Ikeda, Y. Kubota, K. Kato, M. Takata, T. Yamamoto, S. Matsumura, H. Kitagawa, Shape-dependent hydrogen-storage properties in pd nanocrystals: which does hydrogen prefer, octahedron (111) or cube (100)?, Journal of the American Chemical Society 136 (29) (2014) 10222–10225.

[13] G. Li, H. Kobayashi, J. M. Taylor, R. Ikeda, Y. Kubota, K. Kato, M. Takata, T. Yamamoto, S. Toh, S. Matsumura, et al., Hydrogen storage in pd nanocrystals covered with a metal–organic framework, Nature Materials 13 (8) (2014) 802–806.

[14] A. Ulvestad, M. Welland, S. Collins, R. Harder, E. Maxey, J. Wingert, A. Singer, S. Hy, P. Mulvaney, P. Zapol, et al., Avalanching strain dynamics during the hydriding phase transformation in individual palladium nanoparticles, Nature Communications 6 (2015) 1–8.

[15] B. Amin-Ahmadi, D. Connétable, M. Fivel, D. Tanguy, R. Delmelle, S. Turner, L. Malet, S. Godet, T. Pardoen, J. Proost, et al., Dislocation/hydrogen interaction mechanisms in hydrided nanocrystalline palladium films, Acta Materialia 111 (2016) 253–261.

[16] T. C. Narayan, F. Hayee, A. Baldi, A. L. Koh, R. Sinclair, J. A. Dionne, Direct visualization of hydrogen absorption dynamics in individual palladium nanoparticles, Nature Communications 8 (2017) 14020.

[17] A. Ulvestad, M. Welland, W. Cha, Y. Liu, J. Kim, R. Harder, E. Maxey, J. Clark, M. Highland, H. You, et al., Three-dimensional imaging of dislocation dynamics during the hydriding phase transformation, Nature materials 16 (5) (2017) 565–571.

[18] K. Wang, M. Ortiz, M. P. Ariza, Long-term atomistic simulation of hydrogen diffusion in metals, International Journal of Hydrogen Energy 40 (15) (2015) 5353–5358.

[19] Y. Kulkarni, J. Knap, M. Ortiz, A variational approach to coarse graining of equilibrium and non-equilibrium atomistic description at finite temperature, Journal of the Mechanics and Physics of Solids 56 (4) (2008) 1417–1449.

[20] M. P. Ariza, I. Romero, M. Ponga, M. Ortiz, Hotqc simulation of nanovoid growth under tension in copper, International Journal of Fracture 174 (1) (2012) 75–85.

[21] G. Venturini, K. Wang, I. Romero, M. P. Ariza, M. Ortiz, Atomistic long-term simulation of heat and mass transport, Journal of the Mechanics and Physics of Solids 73 (2014) 242–268.

[22] M. Ponga, M. Ortiz, M. P. Ariza, Finite-temperature non-equilibrium quasi-continuum analysis of nanovoid growth in copper at low and high strain rates, Mechanics of Materials 90 (2015) 253–267.

[23] J. Li, S. Sarkar, W. T. Cox, T. J. Lenosky, E. Bitzek, Y. Wang, Diffusive molecular dynamics and its application to nanoindentation and sintering, Physical Review B 84 (5) (2011) 054103.

[24] S. Sarkar, J. Li, W. T. Cox, E. Bitzek, T. J. Lenosky, Y. Wang, Finding activation pathway of coupled displacive-diffusional defect processes in atomistics: Dislocation climb in fcc copper, Physical Review B 86 (1) (2012) 014115.

[25] G. Simpson, M. Luskin, D. J. Srolovitz, A theoretical examination of diffusive molecular dynamics, SIAM Journal on Applied Mathematics 76 (6) (2016) 2175–2195.

[26] X. Sun, M. P. Ariza, K. Wang, Deformation-diffusion coupled analysis of long-term hydrogen diffusion in nanofilms, in: Proceedings of VII European Congress on Computational Methods in Applied Sciences and Engineering, Vol. 1, ECCOMAS, 2016, pp. 197–208.

[27] M. Ponga, M. Ortiz, M. P. Ariza, A comparative study of nanovoid growth in FCC metals, Philosophical Magazine 97 (32, A) (2017) 2985–3007.

[28] J. P. Mendez, M. Ponga, M. Ortiz, Diffusive molecular dynamics simulations of lithiation of silicon nanopillars, Journal of the Mechanics and Physics of Solids 15 (2018) 123–141.

[29] R. A. Miron, K. A. Fichthorn, Accelerated molecular dynamics with the bond-boost method, The Journal of Chemical Physics 119 (12) (2003) 6210–6216.

[30] A. F. Voter, Introduction to the kinetic monte carlo method, in: Radiation Effects in Solids, Springer, 2007, pp. 1–23.

[31] C. S. Martin, M. P. Ariza, M. Ortiz, Modeling thermal conductivity in silicon nanowires, GAMMMitteilungen 38 (2015) 201–212.

[32] E. Dontsova, J. Rottler, C. Sinclair, Solute-defect interactions in al-mg alloys from diffusive variational gaussian calculations, Physical Review B 90 (17) (2014) 174102.

[33] X. Sun, M. P. Ariza, M. Ortiz, K. G. Wang, Long-term atomistic simulation of hydrogen absorption in palladium nanocubes using a diffusive molecular dynamics method, International Journal of Hydrogen Energy 43 (11) (2018) 5657–5667.

[34] E. T. Jaynes, Information theory and statistical mechanics i, Physical Review 106 (4) (1957) 620–630.

[35] E. T. Jaynes, Information theory and statistical mechanics ii, Physical Review 108 (2) (1957) 171–190.

[36] S. R. De Groot, P. Mazur, Non-equilibrium thermodynamics, Courier Corporation, 2013.

[37] X. Sun, M. P. Ariza, M. Ortiz, K. Wang, Acceleration of diffusive molecular dynamics simulations through mean field approximation and subcycling time integration, Journal of Computational Physics 350 (2017) 470–492.

[38] B. Gonzalez-Ferreiro, I. Romero, M. Ortiz, A numerical method for the time coarsening of transport processes at the atomistic scale, Modelling and Simulation in Materials Science and Engineering 24 (4) (2016) 045011.

[39] B. Farmer, M. Luskin, P. Plecháč, G. Simpson, Spin-diffusions and diffusive molecular dynamics, Modelling and Simulation in Materials Science and Engineering 25 (8) (2017) 084003.

[40] J. D. Head, M. C. Zerner, A broyden-fletcher-goldfarb-shanno optimization procedure for molecular geometries, Chemical Physics Letters 122 (3) (1985) 264 – 270.

[41] S. Balay, S. Abhyankar, M. F. Adams, J. Brown, P. Brune, K. Buschelman, L. Dalcin, V. Eijkhout, W. D. Gropp, D. Kaushik, M. G. Knepley, L. C. McInnes, K. Rupp, B. F. Smith, S. Zampini, H. Zhang, H. Zhang, PETSc users manual, Tech. Rep. ANL-95/11 - Revision 3.7, Argonne National Laboratory (2016).
URL `http://www.mcs.anl.gov/petsc`

[42] H. Okuyama, W. Siga, N. Takagi, M. Nishijima, T. Aruga, Path and mechanism of hydrogen absorption at pd (100), Surface Science 401 (3) (1998) 344–354.

[43] A. Zalineeva, S. Baranton, C. Coutanceau, G. Jerkiewicz, Octahedral palladium nanoparticles as excellent hosts for electrochemically adsorbed and absorbed hydrogen, Science Advances 3 (2) (2017) e1600542.

[44] Y. Sakamoto, K. Yuwasa, K. Hirayama, X-ray investigation of the absorption of hydrogen by several palladium and nickel solid solution alloys, Journal of the Less Common Metals 88 (1) (1982) 115–124.

[45] C. Sachs, A. Pundt, R. Kirchheim, M. Winter, M. Reetz, D. Fritsch, Solubility of hydrogen in single-sized palladium clusters, Physical Review B 64 (7) (2001) 075408.

[46] C. Lebouin, Y. Soldo, S. Grigoriev, M. Guymont, P. Millet, Kinetics of hydrogen sorption by palladium nanoparticles, International Journal of Hydrogen Energy 38 (2) (2013) 966–972.

[47] A. L. Bugaev, A. A. Guda, K. A. Lomachenko, V. V. Shapovalov, A. Lazzarini, J. G. Vitillo, L. A. Bugaev, E. Groppo, R. Pellegrini, A. V. Soldatov, et al., Core–shell structure of palladium hydride nanoparticles revealed by combined x-ray absorption spectroscopy and x-ray diffraction, The Journal of Physical Chemistry C 121 (33) (2017) 18202–18213.

[48] X. Zhou, J. A. Zimmerman, B. M. Wong, J. J. Hoyt, An embedded-atom method interatomic potential for pd–h alloys, Journal of Materials Research 23 (03) (2008) 704–718.

[49] M. Ruda, E. Crespo, S. R. de Debiaggi, Atomistic modeling of h absorption in pd nanoparticles, Journal of Alloys and Compounds 495 (2) (2010) 471–475.

[50] C. Lemier, J. Weissmüller, Grain boundary segregation, stress and stretch: effects on hydrogen absorption in nanocrystalline palladium, Acta Materialia 55 (4) (2007) 1241–1254.

[51] Webpage for BlueRidge (Sandy Bridge), `https://secure.hosting.vt.edu/www.arc.vt.edu/computing/blueridge-sandy-bridge/`.

[52] A. Stukowski, Visualization and analysis of atomistic simulation data with ovito–the open visualization tool, Modelling and Simulation in Materials Science and Engineering 18 (1) (2010) 015012.

[53] T. C. Narayan, A. Baldi, A. L. Koh, R. Sinclair, J. A. Dionne, Reconstructing solute-induced phase transformations within individual nanocrystals, Nature Materials 15 (7) (2016) 768–774.

[54] S. Syrenova, C. Wadell, F. A. Nugroho, T. A. Gschneidtner, Y. A. D. Fernandez, G. Nalin, D. Świtlik, F. Westerlund, T. J. Antosiewicz, V. P. Zhdanov, et al., Hydride formation thermodynamics and hysteresis in individual pd nanocrystals with different size and shape, Nature Materials 14 (12) (2015) 1236.

[55] A. Stukowski, Structure identification methods for atomistic simulations of crystalline materials, Modelling and Simulation in Materials Science and Engineering 20 (4) (2012) 045021.

[56] J. Schiøtz, T. Vegge, F. Di Tolla, K. W. Jacobsen, Atomic-scale simulations of the mechanical deformation of nanocrystalline metals, Physical Review B 60 (17) (1999) 11971.

[57] V. Yamakov, D. Wolf, S. R. Phillpot, A. K. Mukherjee, H. Gleiter, Dislocation processes in the deformation of nanocrystalline aluminium by molecular-dynamics simulation, Nature Materials 1 (1) (2002) 45.

[58] P. Wang, S. Xu, J. Liu, X. Li, Y. Wei, H. Wang, H. Gao, W. Yang, Atomistic simulation for deforming complex alloys with application toward twip steel and associated physical insights, Journal of the Mechanics and Physics of Solids 98 (2017) 290–308.

[59] A. Ulvestad, A. Yau, The self-healing of defects induced by the hydriding phase transformation in palladium nanoparticles, Nature Communications 8 (1) (2017) 1376.

[60] S. Plimpton, Fast parallel algorithms for short-range molecular dynamics, Journal of Computational Physics 117 (1) (1995) 1–19.

[61] S. Alekseeva, A. B. S. Fanta, B. Iandolo, T. J. Antosiewicz, F. A. A. Nugroho, J. B. Wagner, A. Burrows, V. P. Zhdanov, C. Langhammer, Grain boundary mediated hydriding phase transformations in individual polycrystalline metal nanoparticles, Nature Communications 8.